J. Fluid Mech. (1983), *vol.* 131, *pp.* 91–122
Printed in Great Britain

Experiments on the transition of homogeneous turbulence to internal waves in a stratified fluid

By D. C. STILLINGER, K. N. HELLAND AND C. W. VAN ATTA†

Institute for Pure and Applied Physical Sciences and Department of Applied Mechanics and Engineering Sciences, University of California, San Diego, La Jolla, CA 92093

(Received 5 July 1982 and in revised form 30 November 1982)

The evolution of unsheared grid-generated turbulence in a stably stratified fluid was investigated in a closed-loop salt-stratified water channel. Simultaneous single-point measurements of the horizontal and vertical velocity and density fluctuations were obtained, including turbulent mass fluxes central in understanding the energetics of the fluctuating motion. When the buoyancy lengthscale was initially substantially larger than the largest turbulent scales, the initial behaviour of the velocity and density fields was similar to that in the non-stratified case. With further downstream development, the buoyancy lengthscale decreased while the turbulence scale grew. Deviations from neutral behaviour occurred when these two lengthscales became of the same order, after the initially larger inertial forces associated with the initial kinetic energy had become weaker and buoyancy forces became important.

Buoyancy forces produced anisotropy in the largest scales first, preventing them from overturning, while smaller-scale isotropic turbulent motions remained embedded within the larger-scale wave motions. These small-scale motions exhibited classical turbulent behaviour and scaled universally with Kolmogorov length and velocity scales. Eventually even the smallest scales of the decaying turbulence were affected by buoyancy, all isotropic motions disappeared, and Kolmogorov scaling failed. The turbulent vertical mass flux decreased to zero for this condition, indicating that the original turbulent field had been completely converted to random internal wave motions.

The transition from a fully turbulent state to one of internal waves occurred rapidly in a time less than the characteristic time of the turbulence based on the largest-scale eddies found in the flow at transition. The dissipation rate for complete transition to a wave field was found to be of the order of $\epsilon_t = 24.5\nu N^2$, where ν is the kinematic viscosity and N the Brunt–Väisälä frequency. This is in fairly good agreement with the value $30\nu N^2$ predicted by Gibson (1980, 1981).

The present experiments have determined quantitative limits on the range of active turbulent scales in homogeneous stratified turbulence, in terms of an upper limit near the buoyancy lengthscale and a lower limit determined by viscosity in the usual way. This description has been used here to help explain and assimilate the results from the earlier stratified grid-turbulence experiments of Lin & Veenhuizen (1975) and Dickey & Mellor (1980). While some of the features of the present observations may be qualitatively seen in the numerical simulations of the problem of Riley, Metcalfe & Weissman (1981), there are fundamental differences, probably due in part to large differences in initial lengthscale ratios and in the limited range of scales attainable in numerical simulations. The present experiments may serve as a useful test case

† Also Scripps Institution of Oceanography.

for future modelling and interpretation of the behaviour of turbulence in stratified flows observed in the oceans and atmosphere.

1. Introduction

Experimental studies have shown that the structure of turbulence and thus the behaviour of mixing processes can be altered by the presence of stable density gradients. Pao (1973) and Lin & Veenhuizen (1975), towing grids in stably stratified water tanks, demonstrated that the vertical component of the turbulent fluctuating velocity field was reduced compared with similar non-stratified flow experiments. They observed that a portion of the turbulent kinetic energy (TKE) was being converted to potential energy as the turbulence did work against the stable gradient. Thus in mixing the fluid a sink for TKE in addition to viscous dissipation was seen to operate. Mainly through flow-visualization techniques it was observed that a rerelease of this potential energy led to slowly decaying internal wave motions capable of radiating energy away from the region of generation.

Tao (1971) and Dickey & Mellor (1980), also using grids towed in salt-stratified water tanks, and Montgomery (1974) using a differentially heated wind tunnel further observed that if the turbulence was vigorous enough then the initial behaviour was influenced very little by buoyancy effects and the initial decay of energy proceeded as in an unstratified flow. Only far downstream were differences seen in either the vertical spectra or fluctuation decay rates. Montgomery (1974) and Lange (1974) also observed the deviation of scalar growth rates from those of non-stratified cases, but again only after the turbulent velocity field had decayed sufficiently such that buoyancy forces were of the same order as the local inertial forces.

These studies document some of the most general features of turbulence decaying in a stably stratified fluid and suggest that the respective strengths of the local inertial and buoyancy forces are important in characterizing the state of the motion. However, the dynamical behaviour of the turbulence during the transition to internal waves, in particular how the various scales of the motion and transport of the active scalar are affected as the energetics of the turbulence changes, remains little understood.

Important differences obviously exist in the two mechanisms by which turbulent kinetic energy can be transformed. Viscous dissipation occurs most effectively at the smallest scales of the motion, while buoyancy suppression originates at the largest scales. The effect on the nonlinear cascade of energy to higher wavenumbers when buoyancy forces suppress the large-scale energy-containing eddies and the relative amounts of kinetic energy lost to these two sinks are matters needing further study. Because of the complexity of the process, there are few models describing decaying turbulence in stratified fluids.

Ozmidov (1965) reviews the early proposed descriptions and gives lengthscale arguments indicating when buoyancy forces should become dynamically important for turbulent motions. A more elaborate development based on Ozmidov's work and the fossil-turbulence concept proposed by Nasmyth (1970) has recently been given by Gibson (1980, 1981). Understanding has been greatly impeded by the lack of controlled experimental studies of turbulence in stratified fluids in which essential information on the energetics of the motion during transition is obtained to test more detailed and generalized models.

The need for more accurate models of stratified turbulence phenomena is clearly evident in the current oceanographic literature. Recent interpretations of micro-

structure measurements from the ocean using various models has led to vastly differing pictures of the energetics of ocean-mixing phenomena (see e.g. Gregg 1980; Caldwell *et al.* 1980; Gibson 1982*a*, *b*).

A primary objective of our research is to stimulate more-quantitative theoretical modelling by experimentally investigating the behaviour of grid-generated turbulence influenced by stable stratification to provide detailed information about the flow during transition to internal waves. The experiments described are extensions of the previously mentioned works in that simultaneous single-point measurements of the fluctuating velocity and density fields were taken in which the variances could be completely resolved such that complete spectral descriptions of the TKE and scalar components as well as the fluxes of these fields could be produced and measured.

These extensions were possible due to the development of a new type of stratified-flow facility and associated instrumentation. This apparatus is described in Stillinger (1981) and in the companion paper by Stillinger *et al.* (1983). This facility produces density-stratified flows lasting for several hours, enabling detailed measurements of the decaying turbulence. Hot-film anemometry combined with a new microscale low-drift four-wire conductivity probe were used to measure simultaneously the mean and fluctuating longitudinal and vertical velocity components and the mean and fluctuating density field. The data will be analysed and compared with the earlier experiments and computations using as a framework the simple theoretical ideas described in §2.

2. Characteristic lengthscales for decaying homogeneous turbulence in a stabilizing mean density gradient

As we are aware of no suitable detailed theoretical calculations with which to compare our experimental results, we shall attempt to interpret our observations in terms of available semiquantitative results based largely on physical arguments about which lengthscales govern the overall behaviour of turbulence in stratified fluids.

The earlier experiments mentioned suggested that various parameters of the flow indicative of the respective strengths of inertial and buoyancy forces at various lengthscales can be used to characterize the fluid motion in its transition from turbulence to internal waves.

Ozmidov (1965) and others realized the existence and importance of a length scale for which buoyancy and inertial forces become of equal importance. He derived a scale size at which buoyancy would affect the overturning turbulent motion and confine the larger scales to horizontal movements. This idea was not new and had appeared independently from several sources (see Monin & Obukhov 1953; Obukhov 1959; Dougherty 1961).

If the buoyancy lengthscale L_b is defined to be the vertical distance travelled by a fluid particle in converting all of its vertical fluctuation kinetic energy into potential energy in a stably stratified fluid with mean vertical density gradient $\partial\bar{\rho}/\partial z$, then one finds

$$L_b = \frac{(\overline{w^2})^{\frac{1}{2}}}{N}, \tag{1}$$

Where $(\overline{w^2})^{\frac{1}{2}}$ is the root-mean-square vertical fluctuation velocity and N is the Brunt–Väisälä frequency

$$N = \left(-\frac{g}{\bar{\rho}}\frac{\partial\bar{\rho}}{\partial z}\right)^{\frac{1}{2}}.$$

L_b would thus set an upper limit for the largest vertical scale of turbulence in a stratified fluid, and eddies of larger scale, inhibited from overturning, would oscillate as internal wave motions. With more assumptions, the buoyancy lengthscale so defined may be expressed in terms of other parameters. Suppose that w is replaced by or assumed proportional to the root mean square of the total velocity fluctuation intensity, $q = (u^2+v^2+w^2)^{\frac{1}{2}}$, and q is assumed to be related to the dissipation rate of turbulent kinetic energy by the usual formula for a fully turbulent flow

$$\epsilon = \frac{Cq^3}{l}, \tag{2}$$

where l is a lengthscale characteristic of the largest scales of the turbulent motion. Then, with $C = 1$ and assuming that $l = L_b \equiv L_R$, the buoyancy lengthscale may be written as the Ozmidov (1965) scale

$$L_R = \left(\frac{\epsilon}{N^3}\right)^{\frac{1}{2}}. \tag{3}$$

The buoyancy length defined in (1) may be used for purely turbulent flow, mixed regimes of turbulence and internal waves, and pure internal-wave fields. If q includes an internal-wave contribution, the dissipation rate of (2) is inappropriate, but might still be applicable if q were representative of a suitably defined 'turbulent' velocity. As will be seen in the data presented here, the evolution of these two lengthscales can be quite different and provide alternative insights into the dynamics of the flow.

From these arguments, one would expect that for a given stability or N, if initially all turbulence scales were much smaller than L_b or L_R, as homogeneous turbulence decays the largest scales or eddies will be the first to become aware of the stabilizing stratification and will eventually stop overturning as the buoyancy scale decreases. Wave–turbulence interactions would occur over a range of scales, but the smallest lengthscales might behave in a manner similar to unstratified motions embedded in the larger-scale internal-wave motions. While viscosity still acts as the sink for these smaller-scale fluctuations, the loss of the energy of larger scales by coupling into wave energy removes the energy source for small-scale motions, destroying the basis of the energy-cascade process to small scales. Assuming that the smaller-scale motions with $L < L_R$ indeed behaved like classical non-stratified turbulence and followed the same statistical laws, Gibson (1981) postulated that the 'active turbulence' can exist at a given scale L only if this scale, which he describes as a wavelength $\lambda \approx L$, is less than the Ozmidov lengthscale but greater than the Kolmogorov viscous lengthscale $L_K = (\nu^3/\epsilon)^{\frac{1}{4}}$, i.e. for

$$1.2L_R \geqslant L \geqslant 15L_K, \tag{4}$$

where the constants were estimated from Richardson-number and classical isotropic-turbulence arguments, respectively. Experimental estimates of these coefficients were first obtained in the present experiments described below.

A simplified lengthscale classification of the fluctuating motions in a stratified fluid is shown in table 1. This is based on the more detailed classification given by Gibson (1981). For the internal-wave field of case 3, $L_R \approx L_K$ implies

$$\epsilon_t \propto \nu N^2 \tag{5}$$

1. *Fully turbulent flow* $L_R > L > L_K$

Largest scale of the motion $L^* < L_R$ everywhere in the flow. Behaviour can be described by the statistical laws of nonstratified turbulence. Efficiently mixes scalar fluid properties.

2. *Combined turbulent/wave field*

Scales with $L_R > L > L_K$ are still actively turbulent, but the largest scales of the flow $L^* > L_R$ have insufficient energy to overturn. Wavelike oscillations result. Reduced ability to mix scalars.

3. *Internal wave field* $L_R \approx L \approx L_K$

No overturning occurs and no turbulent transport of scalar quantities.

TABLE 1. Classification of fluid motion in stratified field

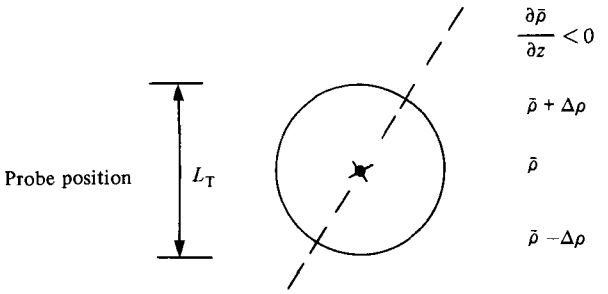

FIGURE 1

as an estimated dissipation rate below which no turbulence exists and only an internal wave field persists. Gibson (1980) has estimated the proportionality constant in (5), obtaining $\epsilon_t = 30\nu N^2$.

Experimental criteria for identifying the state of fluctuating motions in a stratified fluid must be developed in order to test these simple models. By observing the r.m.s. density fluctuation $(\overline{\rho^2})^{\frac{1}{2}}$ and the vertical mass flux $\overline{\rho w}$ as they evolve downstream in our decaying turbulent stratified flow we can establish criteria for determining: (i) when buoyancy forces first begin to affect a turbulent flow that originally is so vigorous that inertial forces dominate all scales of motion and which originally behaves as an unstratified turbulent field, and (ii) when the turbulence becomes completely suppressed by buoyancy forces so that only internal wave motions persist. The first occurs when $(\overline{\rho^2})^{\frac{1}{2}}$ growth departs from non-stratified growth patterns and the second when $\overline{\rho w}$ goes to zero.

If the assumption is made that the ρ-fluctuations are generated from the turbulent entrainment of density across the local density gradient then the lengthscale L_T indicative of the size of the largest overturning motion can also be estimated from the scalar r.m.s. growth curves. By assuming a simple solid-body rotation model for the entrainment process, a density sensor sees a $(\overline{\rho^2})^{\frac{1}{2}}$ r.m.s. fluctuation level if an eddy of scale size L_T entrains fluid across a mean density gradient $\partial\bar{\rho}/\partial z$ as seen in figure 1. Then $\partial\bar{\rho}/\partial z = 2\Delta\rho/L_T$ or

$$L_T = \frac{-2(\overline{\rho^2})^{\frac{1}{2}}}{\partial\bar{\rho}/\partial z}. \tag{6}$$

This scale is a weighted length based on average deviations of density from the mean value $\bar{\rho}$. The actual largest eddy of the turbulent motion may be somewhat different, but this statistical length, which assumes all contributions to ρ are from one lengthscale, will give a consistent indication of the predominant energy-containing scale size. Since the r.m.s. density fluctuation is a convenient quantity to measure in turbulent flows, characteristics of that flow based on such measurements are desirable.

The second criterion, for the suppression of turbulence, is based on the turbulent-transport correlation $\overline{\rho w}$, as suggested by Stewart (1969), who judged it to be perhaps the best diagnostic tool readily available for distinguishing turbulence from waves. Waves are capable of transporting momentum, but cannot overturn and entrain fluid from layers above and below unless they have embedded turbulence. Therefore $\overline{\rho w}$, which is a measure of mass transport, will have near-zero values for a random internal wave field free of turbulent fluctuations.

An energy-equipartition criterion for the transition of turbulence to internal waves can be obtained by equating the vertical kinetic energy per unit volume $\frac{1}{2}\overline{\rho w^2}$ with the mean-square fluctuation potential energy per unit volume $-\frac{1}{2}g(\partial\bar{\rho}/\partial z)^{-1}\overline{\rho^2}$, with the result that

$$\overline{w^2}N = \tfrac{1}{4}L_{\mathrm{T}}^2 N^3, \tag{7}$$

where each of the terms has the same dimensions as ϵ, and may be considered to represent a dissipation rate characteristic of the transition region. The term on the right-hand side of (7) is identical in form with the internal-wave-dissipation model employed by Dickey & Mellor (1980), with L_{T} playing the role of their macroscale Λ.

3. Present experiments

Our experiments to study the behaviour of grid-generated turbulence in a stratified fluid were performed in the UCSD water channel described in the companion paper (Stillinger *et al.* 1983). One of the experiments was non-stratified, using deionized fresh water, while the others used salt brine to produce stable linear density gradients. The fresh-water run was performed to insure that classical decaying turbulent flows could be reproduced in the UCSD facility as well as to assess the background turbulence levels in the facility. Stratified data are compared to this baseline data to emphasize differences due to buoyancy. The experimental parameters pertinent to each run are listed in table 2.

In table 2, $\overline{U}_{\mathrm{CL}}$ indicates mean downstream velocity for a given experiment and N the Brunt-Väisälä frequency. $\overline{U}_{\mathrm{CL}}$ is tabulated for the position of the probes during primary data acquisition. This position was always located on the vertical and transverse centreline of the test section.

Data from a DISA X-film and a microscale-conductivity instrument (MSCI) in close proximity (approx. 1 mm separation) were simultaneously recorded at 10 downstream stations ranging from 10 to 100 mesh lengths from the grid in all experiments. A square-mesh biplane grid with rod diameter $d = 0.318$ cm and spacing $M = 1.905$ cm giving a porosity $M/d = 6$ was used for all runs. The Reynolds number based on the grid mesh size was approximately 4700. The initial uniform mean velocity profile for the fresh- and salt-water runs is shown in figure 2. The three stratified data runs were obtained from one continuous experiment as described in Stillinger *et al.* (1983). The linear density gradients for each stability are shown in figure 3 and represent overall Brunt–Väisälä frequencies of 0.95, 0.73 and 0.45 rad/s.

Type	Experiment number	$\bar{U}_{CL}$ (cm/s)	$\frac{\partial \bar{U}}{\partial z}$ (s^{-1})	$\frac{\partial \bar{\rho}}{\partial z}$ (g/cm^4)	N (s^{-1})
Uniform velocity profile; stable density gradients	23	25.0	0	-9.78×10^{-4} to -1.37×10^{-4}	0.97–0.36
Uniform velocity profile; no density stratification	26	25.6	0	0	0

TABLE 2. Experimental parameters for uniform-flow experiments

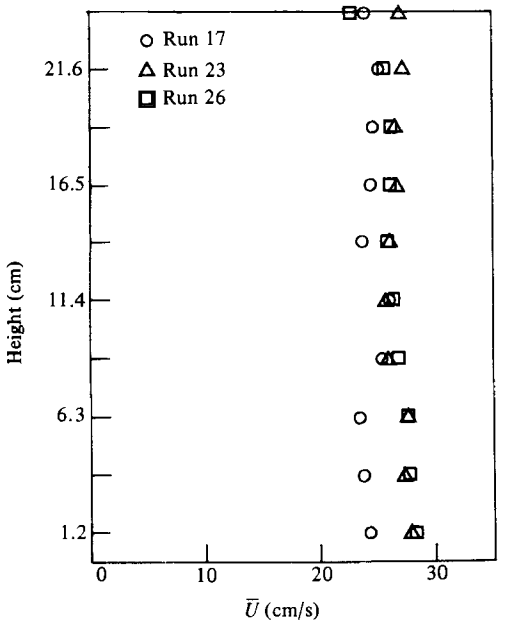

FIGURE 2. Mean-velocity profiles for stratified (run 23) and non-stratified (runs 17 and 26) uniform-flow experiments.

The equations for the variances of the velocity and density fluctuations that apply for the present experimental conditions are

$$\bar{U}\frac{\partial}{\partial x}\frac{\overline{u^2}}{2} + \left[-\frac{1}{\bar{\rho}}\overline{p\frac{\partial u}{\partial x}}\right] + \nu\overline{\left(\frac{\partial u}{\partial x_j}\frac{\partial u}{\partial x_j}\right)} = 0, \tag{8}$$

$$\bar{U}\frac{\partial}{\partial x}\frac{\overline{v^2}}{2} + \left[-\frac{1}{\bar{\rho}}\overline{p\frac{\partial v}{\partial y}}\right] + \nu\overline{\left(\frac{\partial v}{\partial x_j}\frac{\partial v}{\partial x_j}\right)} = 0, \tag{9}$$

$$\bar{U}\frac{\partial}{\partial x}\frac{\overline{w^2}}{2} + \left[-\frac{1}{\bar{\rho}}\overline{p\frac{\partial w}{\partial z}}\right] + \frac{g}{\bar{\rho}}\overline{\rho w} + \nu\overline{\left(\frac{\partial w}{\partial x_j}\frac{\partial w}{\partial x_j}\right)} = 0, \tag{10}$$

$$\left[\quad\right] \longrightarrow = 0$$

$$\bar{U}\frac{\partial}{\partial x}\frac{\overline{\rho^2}}{2} + \overline{\rho w}\frac{\partial \bar{\rho}}{\partial z} + k_\rho\overline{\frac{\partial \rho}{\partial x_j}\frac{\partial \rho}{\partial x_j}} = 0, \tag{11}$$

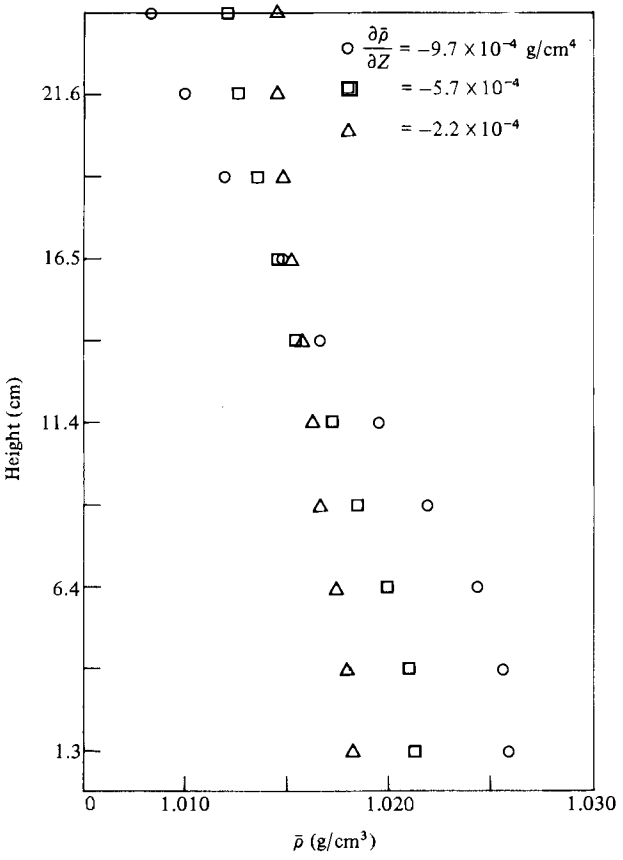

FIGURE 3. Mean-density profiles for run 23.

written for a Cartesian coordinate system with x directed downstream, y transverse and z positive upward. $\overline{U}$ is the mean downstream velocity and is assumed to be constant. u, v, and w are the fluctuating velocity components with zero mean. $\bar{\rho}$ and ρ are the average and fluctuating density. ν and k_ρ are the fluid kinematic viscosity and molecular diffusivity respectively. We note that only the vertical component of the turbulent kinetic energy can have direct sources or sinks due to buoyancy. The pressure–velocity correlations will distribute these effects among all the components. Viscous dissipation ϵ always acts as a sink for the kinetic energy of motion. The first three equations can be combined to form an equation for the TKE $\frac{1}{2}q^2 = \frac{1}{2}(\overline{u^2}+\overline{v^2}+\overline{w^2})$:

$$\overline{U}\frac{\partial}{\partial x}\frac{\overline{q^2}}{2} = -\left(\frac{g}{\bar{\rho}}\overline{\rho w}+\epsilon\right). \tag{12}$$

As observed by Batchelor & Townsend (1948) the present non-stratified data (run 26) obey a linear decay law

$$\frac{\overline{U}^2}{\overline{u_i^2}} = C_i\left[\frac{x}{m}-\left(\frac{x}{m}\right)_0\right], \tag{13}$$

where

$$C_1 = 78.3, \quad \left(\frac{x}{m}\right)_0 = -4.9, \quad \text{and} \quad C_3 = 93.7, \quad \left(\frac{x}{m}\right)_0 = -4.3$$

for $\overline{u^2}$ *and* $\overline{w^2}$ respectively, as plotted in figure 4. The turbulent intensity $(\overline{u_i^2})^{\frac{1}{2}}/\overline{U}$ decayed from about 6.0 % at $x/M = 10$ to 1.0 % at $x/M = 100$. No data were recorded

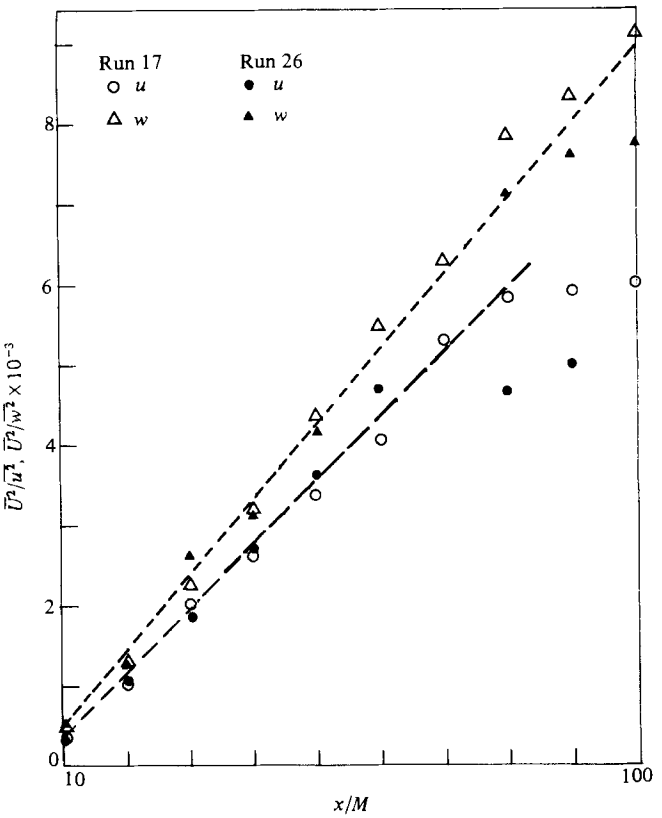

FIGURE 4. Decay of $\overline{u^2}$ and $\overline{w^2}$ behind a biplane grid in a non-stratified uniform flow; $\overline{U} = 25$ cm/s.

beyond station $x/M = 100$, where background turbulence levels are of the order of the decaying fluctuation levels.

The ratio $(\overline{u^2})^{\frac{1}{2}}/(\overline{w^2})^{\frac{1}{2}}$ has maximum values near 1.15, suggesting there are small deviations from isotropy, probably confined to the largest scales.

The effect of adding a stable linear density gradient to the conditions used in the non-stratified flow is shown in figures 5–7, where the effects of buoyancy on the evolution of the variance of velocity fluctuations $\overline{u^2}$ and $\overline{w^2}$ downstream of the grid are clearly seen for the three stratifications of run 23. The linear decay laws found in run 26 are also plotted. As observed by Dickey & Mellor (1980) the behaviour of the turbulent decay directly behind the grid is similar to that of the non-stratified decay. Deviations from this decay rate occur at a downstream location dependent upon the stability of the fluid. The strongest stratification exhibits this deviation nearest the grid. Beyond this point a slower but much more scattered decay occurs, as also observed by Dickey & Mellor (1980).

Figure 8 shows plots of the normalized buoyancy flux $\overline{\rho w}/(\overline{\rho^2})^{\frac{1}{2}}(\overline{w^2})^{\frac{1}{2}}$ versus x/M for each stratification of run 23. A positive value for the correlation indicates turbulent transport in all three cases for stations near the grid. The correlation drops to near zero at a location x/M which decreases with increasing stability of the fluid.

Since $\overline{\rho w}$ will be small in an internal-wave field, the zero-crossing of this transport correlation will be used to estimate the location in the test section where turbulence no longer exists and only internal waves persist.

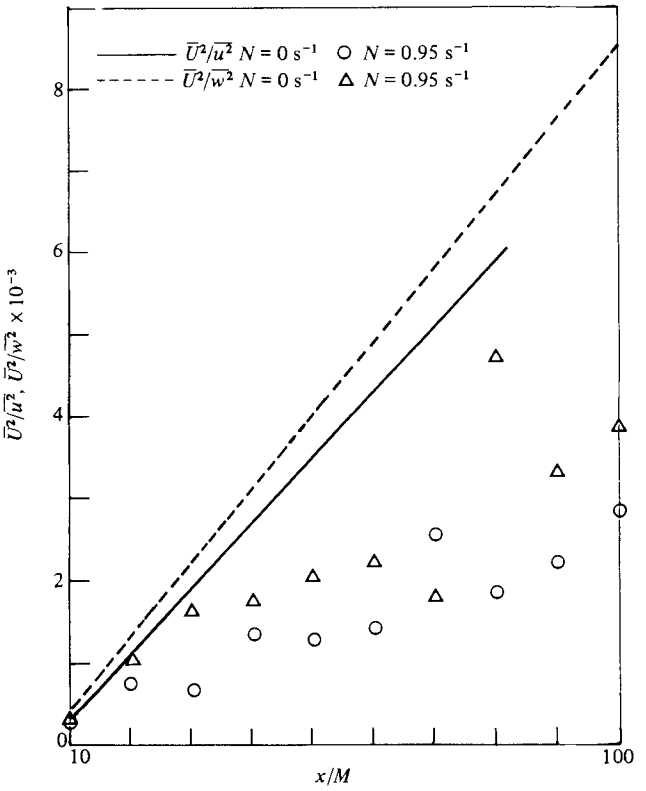

FIGURE 5. Decay of $\overline{u^2}$ and $\overline{w^2}$ for stratified and non-stratified uniform flows; $\overline{U} = 25$ cm/s; runs 23 and 26.

Equation (12) shows that $(g/\bar{\rho})\overline{\rho w}$ and ϵ are the only terms that affect the turbulent kinetic energy of the fluid as the decay proceeds. The ratio of these sinks for TKE is plotted in figure 9. One observes that buoyancy is not very efficient in extracting TKE from the flow with maximum values of $(g/\bar{\rho})\overline{\rho w}$ between 15–20 % of ϵ, the energy being dissipated by viscosity.

The location of maximum potential energy gain occurs farther downstream for weaker stratifications. For these cases reduced buoyancy forces allow the initially turbulent flow to persist farther downstream and thus turbulent mass transport persists. This increased time of overturning motion allows a more complete mixing of the scalar field. For the weaker stratifications very little restratification ($\overline{\rho w} < 0$) is observed, whereas the strongest stability exhibited a large restratification. The restratification produces a rerelease of potential energy into kinetic energy with the transport of fluid particles of given salinity back toward their original equilibrium positions. In the most stable case the suppression of the turbulence occurs such a short period of time after its generation that the mixing of the scalar is incomplete and the restratification occurs. Since the persistence time of the turbulence and thus time allowed for mixing is a function of the initial separation distance of the turbulent and buoyancy lengthscales, a restratification criterion can be based on the ratio L_T/L_R at the time the turbulence is initially generated. Table 3 lists these ratios for run 23 at $x/M = 10$, the station nearest the grid. These data give an estimated upper bound of

$$\frac{L_T}{L_R} \leqslant 0.3 \tag{14}$$

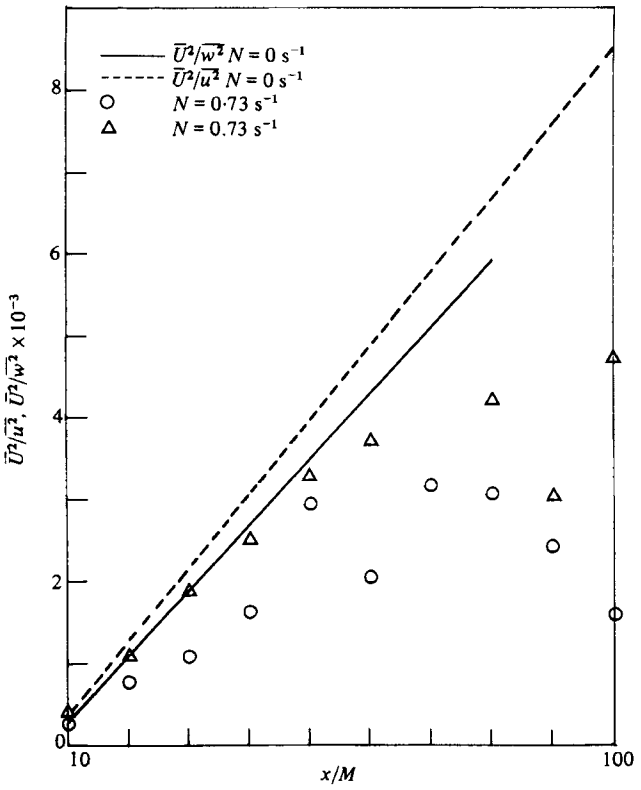

FIGURE 6. Decay of $\overline{u^2}$ and $\overline{w^2}$ for stratified and non-stratified uniform flows: $\overline{U} = 25$ cm/s; runs 23 and 26.

as the criterion for complete mixing. The estimated coefficient of 0.3 is perhaps too large as the initial lengthscale ratio L_T/L_R at the time the turbulence was generated will be somewhat larger than at $x/M = 10$.

Equation (11) states that the evolution of the concentration fluctuations downstream in the channel depends on the competing effects of production due to turbulent interaction with the mean concentration gradient and dissipation due to molecular diffusive forces.

The production of concentration fluctuations is coupled to the velocity field only through the $\overline{\rho w}$ density-flux term in the vertical kinetic energy equation. In strongly turbulent flows $\overline{\rho w}$ will be large and production of density fluctuations will occur as the large-scale eddies entrain fluid across the mean concentration gradient. Montgomery (1974) observed that mean-square passive scalar fluctuations grew with downstream distance as the scales of the turbulence also grew. Under these conditions where passive scalars are mixed by the turbulence, production dominates in (11).

However, as pointed out by Stewart (1969) waves are only capable of transporting momentum and not scalar quantities. The turbulent transport $\overline{\rho w}$ will be small in a wave field and the production term in (11) becomes insignificant. In this extreme case the density fluctuations can only decrease with downstream distance due to the scalar dissipation rate

$$\chi \equiv 2k_\rho \overline{\frac{\partial \rho}{\partial x_j}\frac{\partial \rho}{\partial x_j}},$$

which smears out local gradients of salinity by molecular diffusive action.

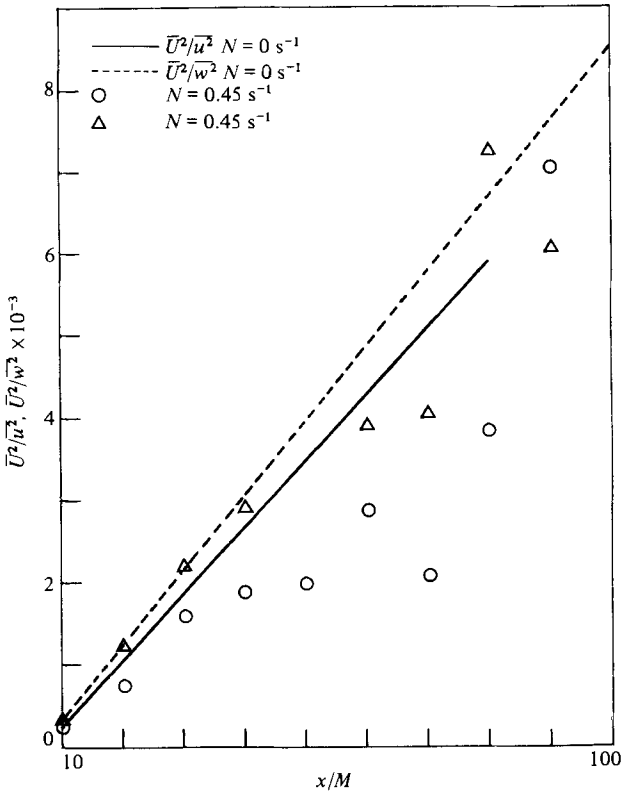

FIGURE 7. Decay of $\overline{u^2}$ and $\overline{w^2}$ for stratified and non-stratified uniform flows; $\overline{U} = 25$ cm/s; runs 23 and 26.

Density fluctuations $(\overline{\rho^2})^{\frac{1}{2}}$ downstream of the grid, normalized to form the overturning scale L_T, are plotted in figure 10 for the three stratifications of run 23 along with the passively heated growth rate observed by Montgomery for temperature in his wind-tunnel study. Montgomery's data was normalized by M/M^*, the ratio of his grid separations to that used in the water channel, since this separation size induces a given initial turbulence scale. Salinity fluctuations $(\overline{\rho^2})^{\frac{1}{2}}$ and therefore L_T grow directly behind the grid in run 23, as do Montgomery's passive temperature fluctuations. However, the growth of our density fluctuations is arrested at some station downstream dependent on the basic stratification. Buoyancy forces inhibit overturning at the largest scales of the turbulent motion, preventing further entrainment across the density gradient and reducing the level of salinity fluctuations. As (11) suggests, a point is reached where production due to turbulent interactions becomes dominated by dissipation as the buoyancy field suppresses the turbulence. These departures from a passive growth law characterize the beginning of a buoyancy-dominated region of motion where previously overturning turbulent scales presumably only oscillate up and down owing to weakening inertial forces compared to local buoyancy forces.

As seen in the velocity fluctuations, weaker stratifications lead to longer periods of passive growth behaviour for $\overline{\rho^2}$. We note that Montgomery's passive stratification yielded a Brunt–Väisälä frequency of $N = 0.8$ s^{-1}, where the present data show active effects for stabilities as low as $N = 0.45$ s^{-1}. This is consistent with the idea that it is the ratio of buoyancy to inertial forces that is important and not the absolute stability of the fluid. Montgomery's grid Reynolds number is an order of magnitude

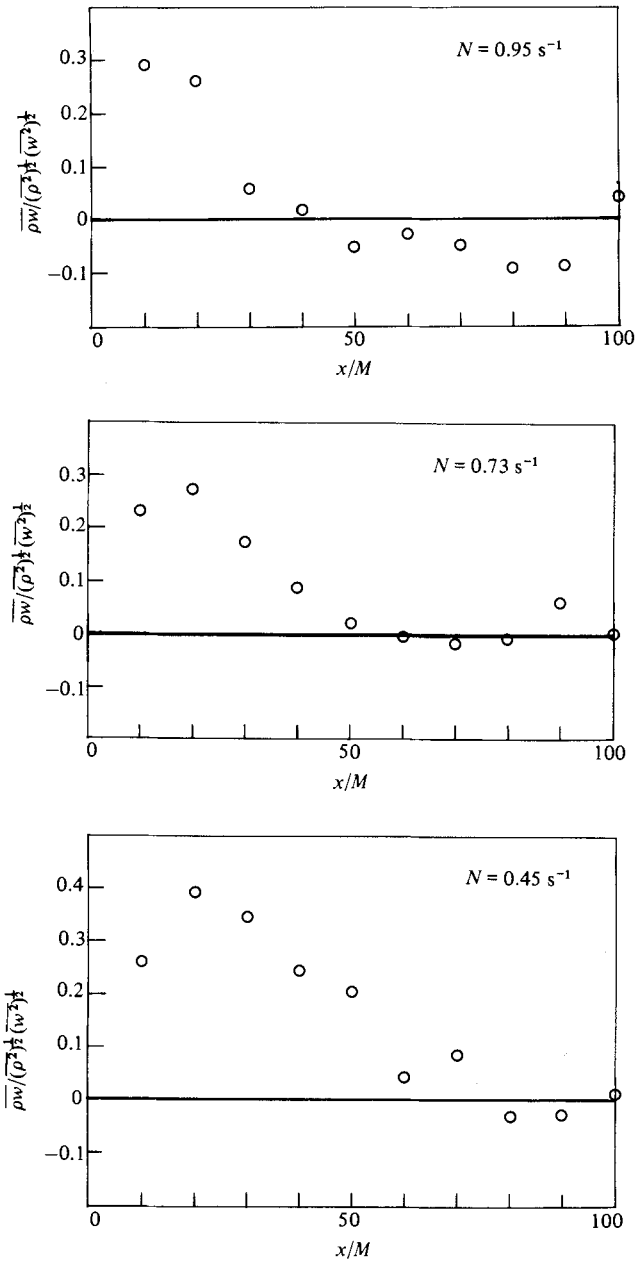

FIGURE 8. Vertical mass flux *vs.* downstream distance for the various stable stratifications of run 23.

higher than for the present study, and the kinetic energy of the turbulence behind his grid was large enough to generate a passive region persisting much further downstream.

The break from a passive growth law indicates when the turbulent field is first affected by the stable stratification. L_T at this transition is used to indicate the size of the largest eddy as buoyancy begins to affect the flow. Numerical tabulations of L_T appear in table 4 for all the stratified runs. Values listed beyond the break in the

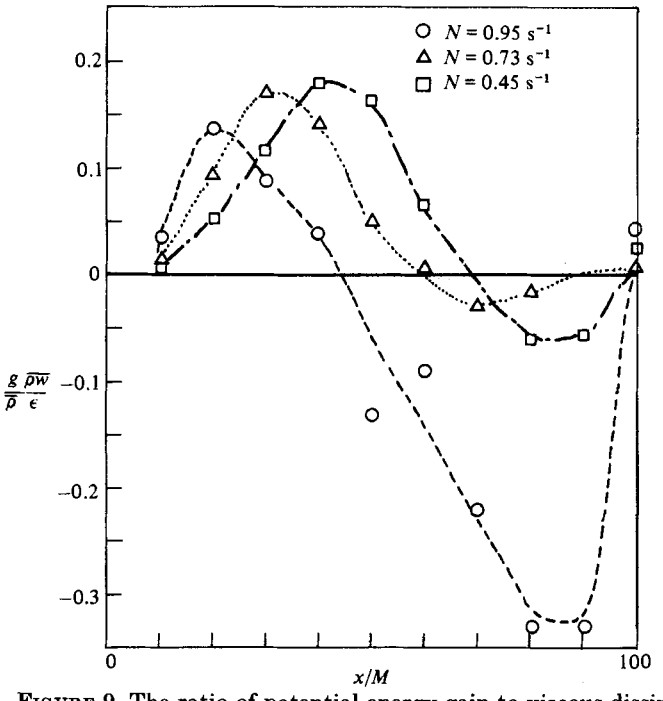

FIGURE 9. The ratio of potential-energy gain to viscous dissipation *vs.* x/M for various stratifications of run 23.

N	L_R	L_T	L_T/L_R	
0.95	2.66	1.17	0.44	Evidence of restratification
0.73	3.64	1.13	0.31	Complete mixing
0.45	7.16	1.16	0.16	Complete mixing

TABLE 3. Initial lengthscales for various stratifications of run 23; $x/m = 10$

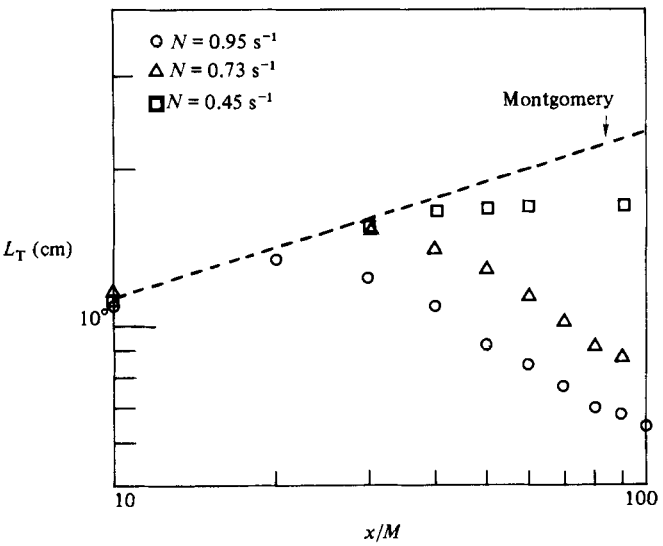

FIGURE 10. Normalized density fluctuations *vs.* downstream distance for stratified uniform flows of run 23: ——, passive temperature fluctuation growth of Montgomery.

growth pattern can no longer be interpreted as an overturning scale once the turbulent field produces large-scale wave motions. In this partial wave state ρ-fluctuation contributions are not restricted to overturning motions, but also come from the wave field. The largest overturning eddy must then be determined from the buoyancy lengthscale L_b.

The same density fluctuation data are plotted in figure 11 as a function of x/MF_r^{-1}, where $F_r = U/NM$ is an overall Froude number based on the mesh size and is an indication of the relative strengths of buoyancy and inertial forces. x/MF_r^{-1} reduces to Nt, a non-dimensional timescale, and represents $1/2\pi$ times the number of Brunt–Väisälä periods downstream based on the local stratification where the data was sampled.

This scaling collapses the data fairly well for $Nt \geqslant 3$ or $\frac{1}{2}$ a Brunt–Väisälä period. In effect, figures 10 and 11 imply that near the grid passive turbulent characteristics are dominated by the grid geometry and thus scale by x/M, but for decaying turbulence under stable stratifications the stabilizing gradient eventually becomes the dominant influence and the fluctuations scale with Nt.

4. Transition lengthscales and criteria for turbulence suppression

In order to quantify the various lengthscale arguments and relations of §2, the lengthscales L_b, L_R, L_T and L_K were calculated and compared for each station at which measurements were taken. The appendix describes the procedure used to obtain ϵ, including the effects of the X-film's spatial resolution. Table 4 lists the various lengthscales and dissipation rates for all the experiments.

The variation of L_b, L_R and L_K with x/M is plotted in figures 12, 13 and 14 respectively for run 23. The largest buoyancy lengths are associated with the weakest stratifications. For each case, L_b decreases smoothly at first with x/M and then begins to oscillate around a more slowly decreasing mean value, apparently indicating the appearance of internal waves as in the Dickey & Mellor experiment. The L_R curves do not exhibit corresponding oscillations, but continue to decrease monotonically. The dissipation rates for all three stratifications are nearly the same at each station, and L_K increases monotonically with x/M as shown in figure 14. As noted in §3, for the three cases of run 23, $\overline{\rho^2}$ and hence L_T systematically deviate from non-stratified behaviour farther downstream as the stable density gradient becomes weaker. A least-squares fit of the passive growth curve yields turbulent lengthscales L_T at the 'break' for the three stratifications as listed in table 5. The ratios L_T/L_b and L_T/L_R when buoyancy is first just affecting the largest scales of the turbulence are also listed. The average values are $L_T/L_b = 1.6$ and $L_T/L_R = 1.4$. The latter is of the same order as the theoretical value (4) estimated by Gibson of $L_T/L_R = 1.2$. These data indicate that a fixed value of the ratio L_T/L_b or L_T/L_R indicates when buoyancy-influenced behaviour begins.

Table 6 is a tabulation of Kolmogorov lengthscales L_K and buoyancy lengthscales L_b and L_R when the transport correlation $\overline{\rho w} = 0$ for the various stratifications of run 23. The ratio L_R/L_K appears to remain constant at this condition. The average value $L_R = 11L_K$ indicates when all scales of the turbulence have been damped, and is used to evaluate ϵ_t in (5). The minimum dissipation rate needed for maintenance of the turbulence then becomes

$$\epsilon_t = 24.5\nu N^2. \tag{15}$$

The Gibson estimate of $\epsilon_t = 30\nu N^2$ is in fairly good agreement with the measured value. Having obtained the experimental ratios of the various lengthscales for

x/M	$\overline{U}$ (cm/s)	$(\overline{u^2})^{\frac{1}{2}}$ (cm/s)	$(\overline{w^2})^{\frac{1}{2}}$ (cm/s)	ϵ (cm^2/s^3)	L_K (cm)
			Biplane-grid decay		
10	25.82	1.527	1.407	7.14	0.018
20	25.28	0.784	0.721	9.95×10^{-1}	0.030
30	25.24	0.558	0.494	3.05×10^{-1}	0.040
40	25.37	0.497	0.457	1.54×10^{-1}	0.047
50	25.48	0.439	0.399	9.9×10^{-2}	0.053
60	25.58	0.439	0.373	6.08×10^{-2}	0.060
70	25.79	0.433	0.390	4.84×10^{-2}	0.063
80	25.7	0.377	0.305	3.48×10^{-2}	0.068
90	25.7	0.366	0.295	2.79×10^{-2}	0.072
100	25.82	0.392	0.294	2.34×10^{-2}	0.075
			Vertical-rod-grid decay		
10	24.02	1.44	1.21		
20	24.68	0.832	0.659		
30	24.73	0.614	0.506		
40	24.60	0.526	0.428		
50	24.83	0.529	0.380		
60	24.87	0.465	0.352		
70	24.86	0.472	0.349		
80	24.98	0.507	0.351		
90	25.02	0.517	0.362		
100	25.12	0.507	0.359		

TABLE 4(*a*). Run 26, non-stratified flow statistics; uniform velocity profile

x/M	$\overline{U}$ (cm/s)	$(\overline{u^2})^{\frac{1}{2}}$ (cm/s)	$(\overline{w^2})^{\frac{1}{2}}$ (cm/s)	$\bar{\rho}$ (g/cm^3)	$(\overline{\rho^2})^{\frac{1}{2}}$ (g/cm^3)	$\dfrac{\overline{\rho u}}{(\overline{\rho^2})^{\frac{1}{2}}(\overline{u^2})^{\frac{1}{2}}}$	$\dfrac{\overline{\rho w}}{(\overline{\rho^2})^{\frac{1}{2}}(\overline{w^2})^{\frac{1}{2}}}$	$\partial\bar{\rho}/\partial z$ (g/cm^4)
				Biplane-grid decay				
10	23.72	1.479	1.335	1.01933	0.00057	0.038	0.296	-9.776×10^{-4}
20	23.43	0.859	0.723	1.01954	0.00062	−0.101	0.260	-9.776×10^{-4}
30	23.33	0.916	0.581	1.01965	0.00061	−0.086	0.060	-9.776×10^{-4}
40	23.48	0.628	0.560	1.01958	0.00054	−0.103	0.019	-9.776×10^{-4}
50	23.61	0.661	0.523	1.01939	0.00045	−0.031	−0.056	-9.691×10^{-4}
60	23.83	0.635	0.508	1.01922	0.00041	−0.018	−0.032	-9.691×10^{-4}
70	24.18	0.476	0.567	1.01908	0.00037	−0.075	−0.05	-9.691×10^{-4}
80	24.54	0.568	0.357	1.01886	0.00034	−0.02	−0.091	-9.691×10^{-4}
90	24.52	0.520	0.425	1.01867	0.00030	0.007	−0.086	-8.62×10^{-4}
100	24.89	0.465	0.399	1.01849	0.00028	0.005	0.049	-8.62×10^{-4}
				Biplane grid decay				
10	25.13	1.551	1.421	1.01722	0.00037	0.091	0.230	-6.55×10^{-4}
20	24.67	0.903	0.748	1.01719	0.00042	−0.033	0.279	-6.55×10^{-4}
30	25.75	0.785	0.599	1.01713	0.00043	−0.089	0.173	-5.67×10^{-4}
40	24.79	0.609	0.495	1.01709	0.00040	−0.151	0.092	-5.67×10^{-4}
50	25.16	0.462	0.437	1.01707	0.00036	−0.144	0.026	-5.57×10^{-4}
60	25.23	0.555	0.414	1.01707	0.00032	−0.101	−0.002	-5.57×10^{-4}
70	25.54	0.453	0.315	1.01702	0.00028	−0.082	−0.014	-5.37×10^{-4}
80	25.45	0.464	0.392	1.01703	0.00025	−0.108	−0.006	-5.37×10^{-4}
90	25.44	0.515	0.460	1.01697	0.00022	−0.118	0.069	-5.09×10^{-4}
100	25.64	0.642	0.372	1.01692	0.00022	−0.059	0.007	-4.12×10^{-4}

TABLE 4(*b*). Run 23, stratified-flow statistics; uniform velocity profile

x/M	$\bar{U}$ (cm/s)	$(\overline{u^2})^{\frac{1}{2}}$ (cm/s)	$(\overline{w^2})^{\frac{1}{2}}$ (cm/s)	$\bar{\rho}$ (g/cm^3)	$(\overline{\rho^2})^{\frac{1}{2}}$ (g/cm^3)	$\dfrac{\overline{\rho u}}{(\overline{\rho^2})^{\frac{1}{2}}(\overline{u^2})^{\frac{1}{2}}}$	$\dfrac{\overline{\rho w}}{(\overline{\rho^2})^{\frac{1}{2}}(\overline{w^2})^{\frac{1}{2}}}$	$\partial\bar{\rho}/\partial z$ (g/cm^4)
				Biplane-grid decay				
10	25.47	1.484	1.407	1.01614	0.00015	0.024	0.266	-2.59×10^{-4}
20	25.04	0.920	0.719	1.01614	0.00017	−0.024	0.397	-2.59×10^{-4}
30	25.20	0.646	0.529	1.01610	0.00018	−0.09	0.348	-2.40×10^{-4}
40	25.18	0.584	0.469	1.01608	0.00019	−0.107	0.244	-2.25×10^{-4}
50	25.42	0.571	0.308	1.01607	0.00018	−0.084	0.201	-2.10×10^{-4}
60	25.43	0.474	0.406	1.01605	0.00018	−0.107	0.043	-2.10×10^{-4}
70	25.48	0.561	0.4	1.01604	0.00016	−0.123	0.092	-1.62×10^{-4}
80	25.79	0.417	0.301	1.01602	0.00015	−0.111	−0.034	-1.62×10^{-4}
90	—	0.307	0.331	1.01602	0.00014	−0.057	−0.026	-1.62×10^{-4}
100	—	0.256	0.225	1.01602	0.00013	—	0.013	-1.37×10^{-4}

TABLE 4(*c*). Run 23, stratified-flow statistics; uniform velocity profile

x/M	ϵ (cm^2/s^3)	N (s^{-1})	L_T (cm)	L_K (cm)	L_b (cm)	L_R (cm)
			Biplane-grid decay			
10	6.45	0.9693	1.17	0.020	1.38	2.66
20	7.69×10^{-1}	0.9693	1.27	0.034	0.75	0.919
30	2.22×10^{-1}	0.9680	1.25	0.046	0.60	0.495
40	1.25×10^{-1}	0.9665	1.10	0.053	0.58	0.372
50	9.72×10^{-2}	0.9652	0.93	0.056	0.54	0.329
60	6.40×10^{-2}	0.9652	0.85	0.062	0.66	0.267
70	4.47×10^{-2}	0.9500	0.76	0.068	0.60	0.228
80	3.27×10^{-2}	0.9300	0.70	0.074	0.38	0.202
90	2.99×10^{-2}	0.9106	0.70	0.075	0.47	0.199
100	2.49×10^{-2}	0.9106	0.65	0.079	0.44	0.182
			Biplane-grid decay			
10	6.63	0.7941	1.13	0.019	1.79	3.64
20	8.61×10^{-1}	0.7600	1.28	0.032	0.98	1.40
30	2.45×10^{-1}	0.7390	1.51	0.044	0.81	0.779
40	1.22×10^{-1}	0.7350	1.41	0.052	0.67	0.554
50	7.32×10^{-2}	0.7322	1.29	0.059	0.60	0.432
60	5.89×10^{-2}	0.7200	1.15	0.062	0.58	0.397
70	4.06×10^{-2}	0.7190	1.04	0.068	0.44	0.331
80	3.32×10^{-2}	0.7100	0.93	0.072	0.55	0.305
90	2.81×10^{-2}	0.7000	0.86	0.075	0.66	0.286
100	2.16×10^{-2}	0.637	1.05	0.080	0.58	0.289
			Biplane-grid decay			
10	6.42	0.500	1.16	0.019	2.81	7.16
20	8.80×10^{-1}	0.500	1.31	0.031	1.44	2.65
30	2.72×10^{-1}	0.481	1.50	0.042	1.10	1.56
40	1.16×10^{-1}	0.465	1.68	0.052	1.01	1.07
50	6.49×10^{-2}	0.450	1.71	0.060	0.68	0.844
60	4.47×10^{-2}	0.420	1.71	0.066	0.97	0.777
70	3.38×10^{-2}	0.395	1.97	0.070	1.01	0.741
80	2.35×10^{-2}	0.395	1.85	0.077	0.76	0.618
90	1.83×10^{-2}	0.395	1.73	0.082	0.84	0.545
100	1.55×10^{-2}	0.364	1.90	0.085	0.62	0.567

TABLE 4(*d*). Experimental parameters: run 23 stratified flow, uniform velocity profile

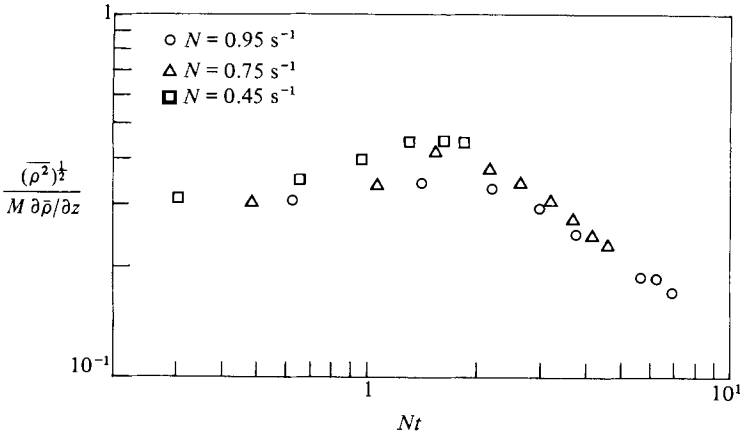

FIGURE 11. Density (salinity) fluctuations *vs.* non-dimensional time based on the fluid stability; run 23.

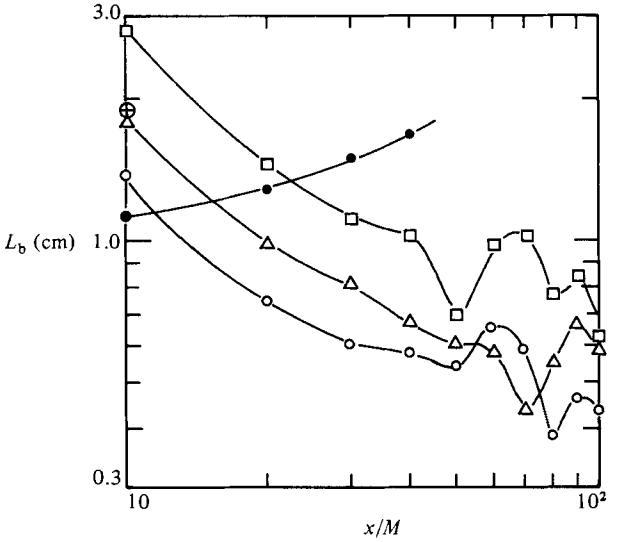

FIGURE 12. Buoyancy lengthscale *vs.* normalized downstream distance for the three stabilities of run 23: ○, $N = 0.95$ rad/s; △, 0.73; □, 0.45; ⊕, grid mesh size M; ●, L_T.

specific states of the motion, the experimentally determined version of (4) becomes

$$1.4L_R \geqslant L \geqslant 15.4L_K, \tag{16}$$

giving the range of active turbulent scales in homogeneous stratified turbulence.

Figure 15 is a lengthscale evolution 'map' based on (16) for all stratifications of run 23. A similar map may be constructed using L_b. This map graphically illustrates the three locations in the water-channel test section where turbulence begins its transition into waves depending on the magnitude of the mean density gradient. The intersections where $1.4L_R$ is equal to the passive scalar L_T value at $x/M = 18$ for $N = 0.95$ s^{-1}, $x/M = 27$ for $N = 0.73$ s^{-1}, and $x/M = 37$ for $N = 0.45$ s^{-1} correspond to the breaks from passive growth behaviour. The evolution of the measured L_T beyond these intersections is given in figure 10. Complete suppression of the turbulence is predicted at $x/M = 30$ for $N = 0.95$ s^{-1}, $x/M = 40$ for $N = 0.73$ s^{-1} and $x/M = 60$ for $N = 0.45$ s^{-1}, consistent with locations where the buoyancy flux $\overline{\rho w}$

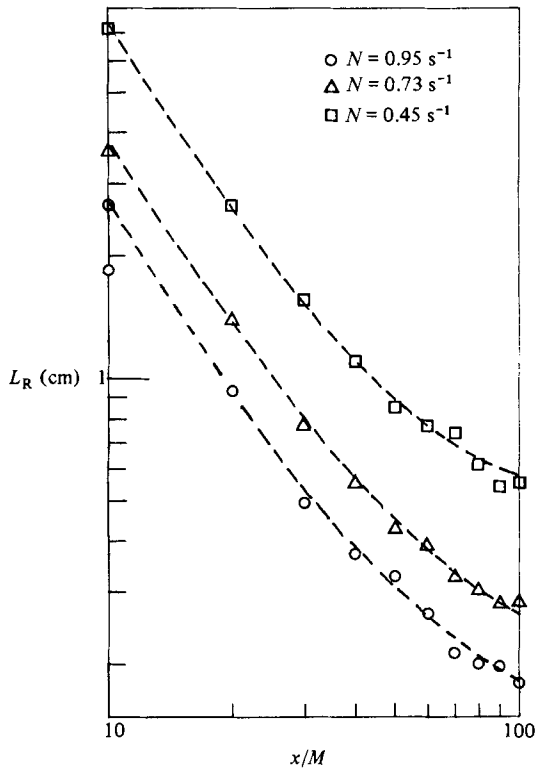

FIGURE 13. Ozmidov lengthscale L_R *vs.* normalized downstream distance for the three stabilities of run 23. Nomenclature same as for figure 12.

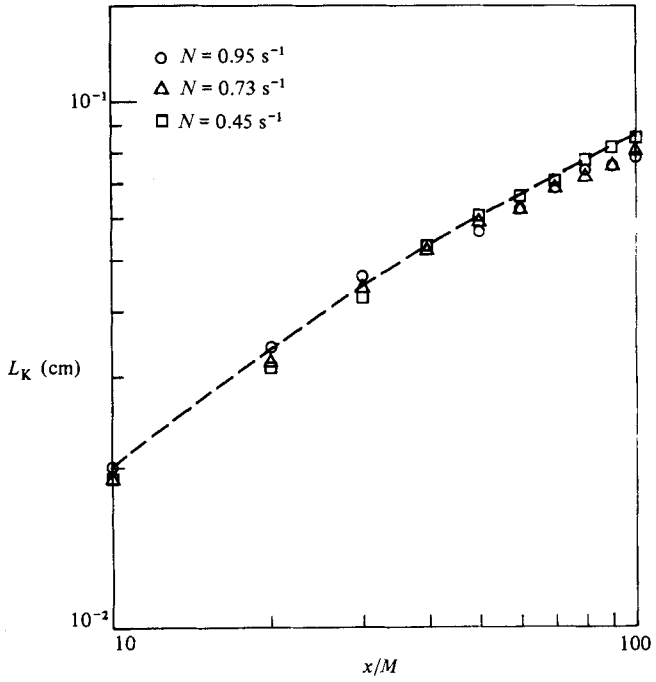

FIGURE 14. Kolmogorov lengthscale *vs.* downstream distance for the three stabilities of run 23.

N (s^{-1})	x/M	L_T (cm)	L_T/L_b	L_R (cm)	L_T/L_R
0.95	18	1.25	1.56	1.02	1.22
0.73	27	1.45	1.70	0.90	1.61
0.45	37	1.62	1.57	1.20	1.35

TABLE 5. Lengthscales for various stratifications when buoyancy forces first affect the turbulence; run 23

N (s^{-1})	x/M	L_b (cm)	L_b/L_K	L_R (cm)	L_R/L_K
0.95	30	0.6	13.0	0.495	10.7
0.73	40	0.67	12.9	0.554	10.65
0.45	60	0.97	14.7	0.777	11.7

TABLE 6. Lengthscales when $\overline{pw} = 0$ for various stratifications of run 23

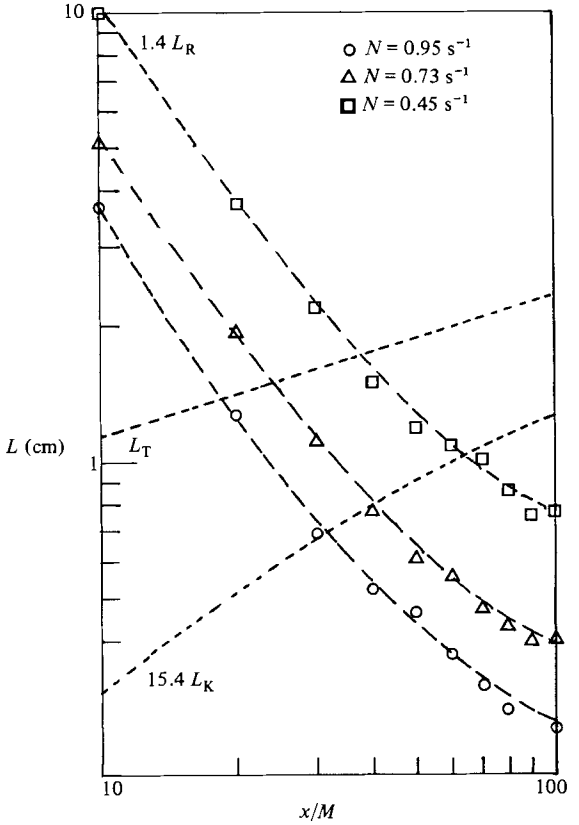

FIGURE 15. Lengthscale evolution map for the three stably stratified turbulent flows of run 23.

approaches zero. The fixed ratio of buoyancy, inertial and viscous lengthscales as indicated by (16) appears to describe the behaviour of the turbulence in these experiments.

Figure 16 is a graphical summary of the behaviour of homogeneous turbulence with $L_R \gg L_T$ initially at various stations downstream of the grid for a fixed value of N.

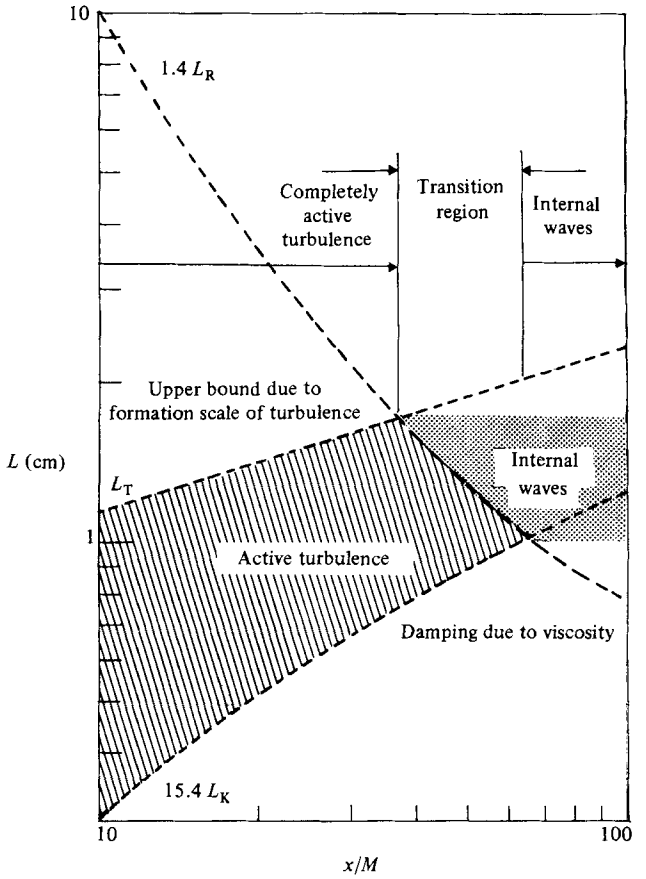

FIGURE 16. Evolution map for homogeneous turbulence in a stably stratified fluid with $L_T \ll L_R$ initially.

A similar map may be drawn using L_b instead of L_R. A spectrum of turbulent scales from L_K to L_T initially exists at $x/M = 0$, determined by the grid Reynolds number and initial dissipation rate. Since inertial forces dominate buoyancy forces at these scales, in the initial region behind the grid both scales L_T and L_K grow as in classical non-stratified decaying homogenous turbulence. A change or break from classical non-stratified behaviour will occur when the dissipation rate ϵ has decreased sufficiently and the largest scale L_T of the turbulence has grown to a value of about $1.4L_R$. This ratio can be achieved with different dissipation rates and stratifications, so dynamically significant buoyancy effects will occur at a location dependent on the energetics of the system, but the critical ratio of these scales remains fixed.

When $L_R \approx 11L_K$ turbulent processes no longer occur as all turbulent eddies have been damped either by buoyancy or viscosity. The time of transition from fully turbulent fluctuations to a field having only wave motion depends on the specific flow conditions, but the onset and completion are characterized by a fixed ratio of the pertinent scales.

To examine the energy-equipartition transition criterion of (7), $\overline{w^2}N$ and $\frac{1}{4}L_T^2 N^3$ are compared in figure 17 for the three cases of run 23. At $x/M = 10$, the vertical kinetic energy is five to twenty times larger than the fluctuating potential energy. The two energies approach one another as x/M increases, and initial equality is achieved at a value of x/M which increases with decreasing N. At the point where $\overline{\rho w} = 0$, the

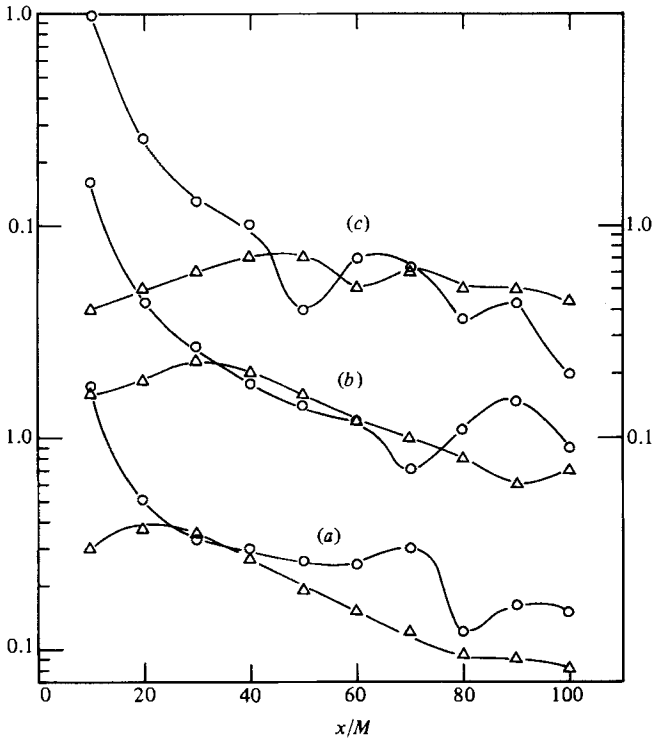

FIGURE 17. Comparison of vertical kinetic energy with fluctuating potential energy: ○, $\overline{w^2}N$; △, $\frac{1}{4}L_T^2N^3$; (*a*) $N = 0.95$; (*b*) 0.73; (*c*) 0.43.

ratios of $\overline{w^2}N$ to $\frac{1}{4}L_T^2N^3$ are 1.1, 1.0 and 1.1 for $N = 0.95$, 0.73 and 0.45 respectively. For larger x/M, the differences are larger, owing partially to the large undulations in $\overline{w^2}$ in the wave region. For the most-stratified case, $\overline{w^2}N$ is systematically larger than $\frac{1}{4}L_T^2N^3$ in the region where the largest restratification is observed, consistent with the conversion of potential energy into kinetic energy associated with the negative buoyancy flux. The equipartition criterion appears to be a useful indicator for defining the transition region and associated dynamical features.

5. Transition energy spectra

Vertical velocity spectra non-dimensionalized by Kolmogorov length and velocity scales are plotted in figure 18. These plots compare several stations of non-stratified data from run 26 with the weakest stratification of run 23, which exhibits transition over the largest region in the channel.

These plots reveal the behaviour of the various scales during transition. Near the grid (figure 18*a*) universal similarity appears to be maintained over all scales in the flow where the lengthscale arguments predict that buoyancy forces should be ignored. Figure 18(*f*) shows that similarity also holds for downstream stations in the non-stratified flow. Figures 23 and 24 show that this non-stratified data collapses to that for a high-Reynolds-number flow in air. Figures 18 (*b–e*) then reveal that the large scales are in fact the first to be suppressed by buoyancy forces and that the lengthscales L_R predict this deviation as theorized by Ozmidov (1965) and Gibson (1980). Smaller scales still seem to exhibit similarity as predicted until $1.4L_R$ becomes of the order of $15L_K$. Similarity then appears to fail at all scales, a result which should

be viewed cautiously in the large-wavenumber region where the spectral levels approach the noise.

The transition state defined by the length of time any turbulence persists after buoyancy suppresses the largest eddies is observed to be of very short duration. Table 7 lists lifetimes based on the data of run 23. The transition region appears to exist for about 0.15 Väisälä periods in all cases. The characteristic time of the turbulence at the beginning of transition $t = L_T/(\overline{u^2})^{\frac{1}{2}}$, where $(\overline{u^2})^{\frac{1}{2}}$ is the root-mean-square longitudinal turbulence intensity, is also listed in table 7 and shows that complete collapse of the turbulence occurs in less than one characteristic overturning of the energy-supplying eddies. This seems consistent with observations of Lange (1974) and other investigators, who have observed the collapse of turbulent motion within one cycle of the generating event when buoyancy dominates at the largest scales.

6. Discussion and interpretation of earlier experiments and numerical simulations

The present results were obtained in a relatively low-Reynolds-number flow ($Re_m = 4700$). In order to test our conclusions further, they will first be compared with the high-Reynolds-number ($Re_m = 48260$) experiment of Dickey & Mellor (1980). Their results from towing a grid vertically through a column of salt-stratified water at high speed (95 cm/s) showed that the decay of turbulent kinetic energy $\frac{1}{2}\overline{q^2}$ for neutral and stratified ($\partial\overline{\rho}/\partial z = 1.4 \times 10^{-4}$ g/cm^4, $N = 0.378$ s^{-1}) cases were identical until $x/M = 250$–275. The vertical velocity component $(\overline{w^2})^{\frac{1}{2}}$ deviated from neutral decay behaviour slightly sooner than the horizontal component $(\overline{u^2})^{\frac{1}{2}}$. Both components showed slowly decaying irregular behaviour beyond this break, indicative of internal wave motions.

A characteristic lengthscale evolution map compiled from the Dickey & Mellor data, extrapolating when necessary, is given in figure 19. They did not measure the density fluctuations or L_T. The observed lengthscale behaviour and our interpretation is very similar to that for our experimental data. Right behind the grid, at $x/M = 10$, the buoyancy length is about a factor of five larger than the grid mesh size. Buoyancy forces probably first become important for values of x/M when $L_b \approx L_R \approx L_T$. For $x/M > 275$, L_b begins to oscillate erratically as for our data and L_R drops rapidly owing to the decreased dissipation rate of the internal-wave field. The transition to an internal-wave field at $x/M \approx 275$ occurs when L_b, $1.4L_R$ and $15.4L_K$ are all nearly equal. The turbulent Froude numbers L_b/λ and L_R/λ (where λ is the Taylor microscale) at the crossover point are 1.1 and 0.6 respectively, the latter being fairly close to the corresponding average value of 0.87 for our data. The crossover station where $L_R/L_K = 11$ is at $x/M = 240$, so the criterion based on (5) suggests that all turbulent motions have been suppressed beyond this station and the dissipation rate has dropped below the critical transition value of $\epsilon_t = 24.5\nu N^2 = 0.035$ cm^2/s^3. According to the dissipation-rate calculations of Dickey & Mellor, the transition dissipation rate is observed to be

$$0.025 < \epsilon_t < 0.035 \text{ cm}^2/\text{s}^3,$$

so (15) produces a good estimate for the point of transition of this high-Reynolds-number stratified-grid turbulence to internal wave motions. However, as illustrated by the precipitous behaviour of L_R in figure 19, the Dickey & Mellor dissipation rate for $x/M > 275$, as estimated roughly from a fit to the decay of kinetic energy in that

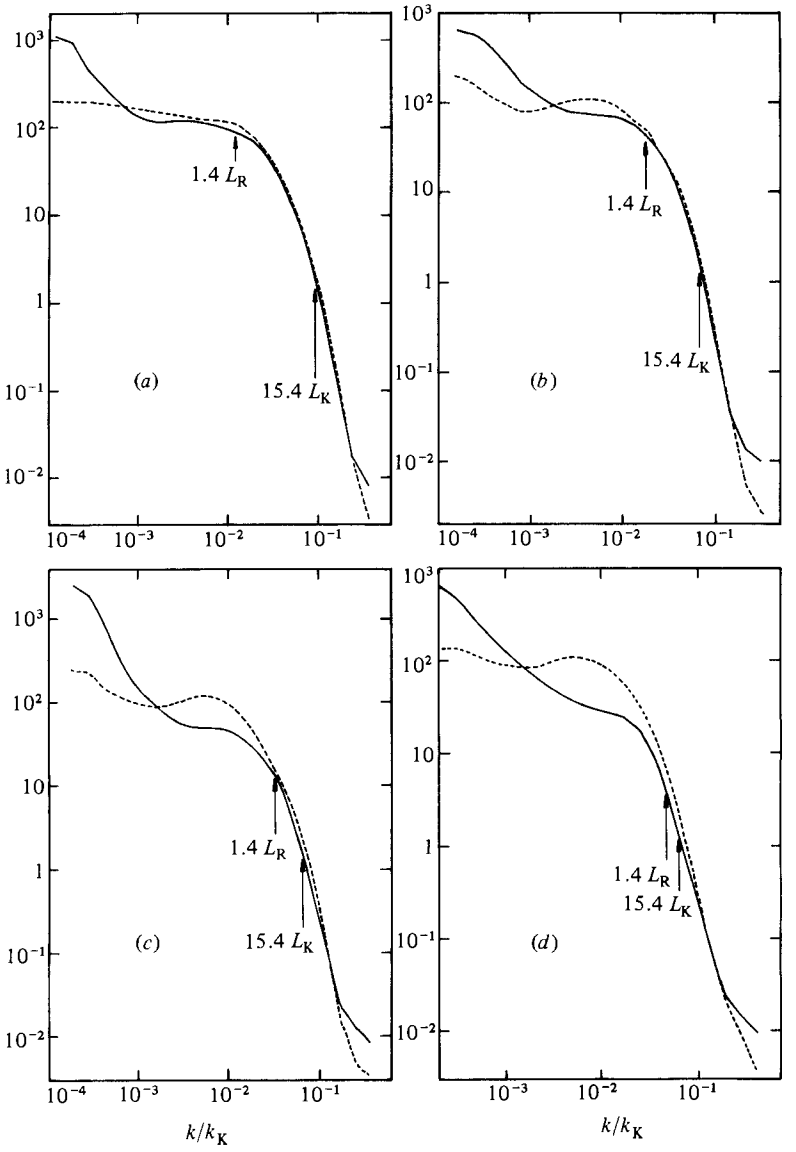

FIGURE 18 (*a–d*). For caption see facing page.

region, drops very quickly to a value near 0.0038 cm^2/s^3, a factor of nearly 10 smaller than that immediately before transition to an internal-wave field and the estimate of (15).

A lengthscale evolution map for the Lin & Veenhuizen data is given in figure 20. The observed behaviour is quite different from the cases discussed above. The buoyancy lengthscales L_b and L_R, and the overturning scale L_T, are initially all nearly equal just downstream of the grid, so that the turbulence is strongly influenced by buoyancy forces throughout the entire decay period. The crossings of the L_b and L_R curves with that of $15.4L_K$ does not result in the characteristic erratic-wave-like behaviour of L_b, or in a rapid change in the dissipation rate or rate of decay of the fluctuations as in our experiments and that of Dickey & Mellor, both of which had an initially relatively large separation of buoyancy and overturning lengthscales.

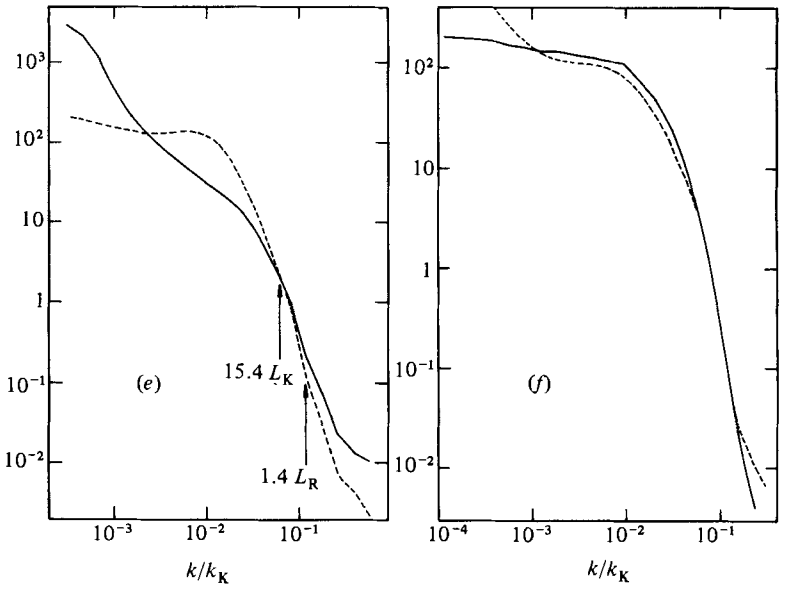

FIGURE 18. Normalized vertical velocity spectra $k_K E(k)/v_K^2$. —, $N = 0.45$ rad/s, run 23; – – – –, $N = 0$, run 26. (*a*) $x/M = 20$; (*b*) 30; (*c*) 40; (*d*) 50; (*e*) 100; (*f*) $N = 0$; —, $x/M = 20$; – – – –, $x/M = 60$.

N (s^{-1})	0.95	0.73	0.45
Time of transition T (s)	1	1.2	2.0
$TN/2\pi$	0.15	0.14	0.143
L_T at transition (cm)	1.35	1.55	1.70
Turbulence time $t = L_T/(\overline{u^2})^{\frac{1}{2}}$ (s)	1.5	1.9	2.8

TABLE 7. Transition times for the various stratified turbulent decays

According to the present lengthscale arguments, active turbulence has been completely damped by about $x/M = 18$, and therefore most of the Lin & Vennhuizen data may represent a random decaying internal-wave field.

Decay rates for $\overline{w^2}$ and $\overline{\rho^2}$, the variances of vertical velocity and density, were observed to have the same power-law dependence, and the authors propose that this may imply an equal partitioning of kinetic and potential energy indicative of internal-wave motions. This proposal is examined in figure 21, in which the vertical kinetic energy and fluctuating potential energy terms of the equipartition equation (7) are plotted versus x/M for their data. The two terms are nearly equal right behind the grid, but the ratio of $\overline{w^2}N$ to $\frac{1}{4}L_T^2 N^3$ grows as x/M increases, reaching 3.5 at $x/M = 100$. This behaviour is very similar to that observed in our data of figure 17 for $N = 0.95$, the most highly stratified case, beyond the point where $\overline{\rho w} = 0$. There is no equipartition of energy in the wave regime, but the results are consistent with our data and with their estimates that the buoyancy flux was nearly zero for their experiment. Dissipation rates that are less than $24.5\nu N^2$ for their stations beyond $x/M = 18$ further reinforce this conclusion.

A numerical simulation of decaying stratified, initially isotropic turbulence has been carried out by Riley, Metcalfe & Weissman (1981). An initially isotropic homogeneous turbulence with no buoyancy forces was allowed first to develop and decay normally in time, and then at a given time of development the buoyancy field

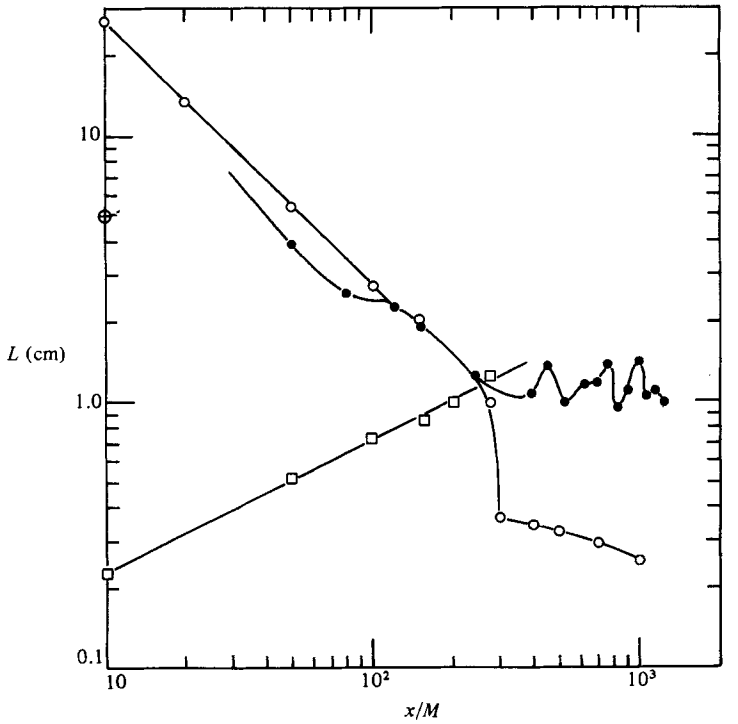

FIGURE 19. Lengthscale evolution map for the data of Dickey & Mellor (1980): ●, L_b; ○, $1.4L_R$; □, $15.4L_K$; ⊕, M.

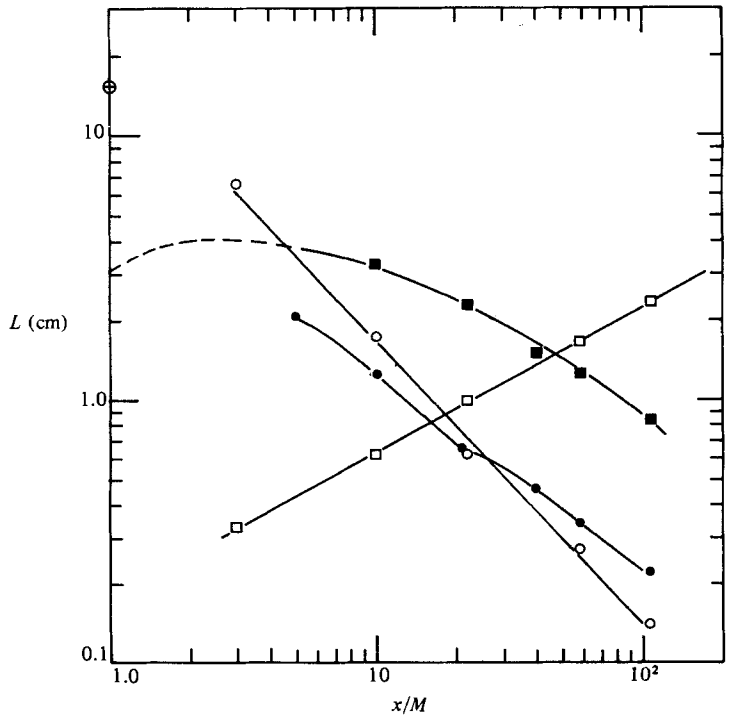

FIGURE 20. Lengthscale evolution map for the data of Lin & Veenhuizen (1975): ■, L_T; other nomenclature same as in figure 19.

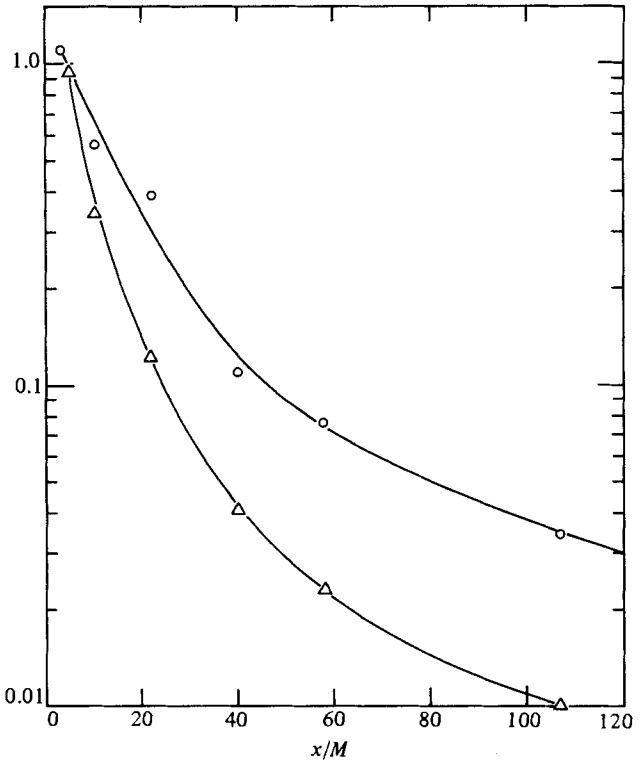

FIGURE 21. Comparison of vertical kinetic energy with fluctuating potential energy for data of Lin & Vennhuizen (1975): ○, $\overline{w^2}N$; △, $\frac{1}{4}L_T^2N^3$.

was 'turned on'. The qualitative behaviour of the simulation results is in some respects very similar to that observed in our experiments. The buoyancy flux $\overline{\rho w}$ and density-fluctuation intensity $\overline{\rho^2}$, which were initially zero, increase smoothly to maximum values and then decay toward zero, and for the most highly stratified case a counter-gradient density flux produced by the negative overshoot of $\overline{\rho w}$ is observed. However, in the simulations the transition to an internal-wave field was not characterized by any abrupt changes in the dissipation rate or in the decay rate of the velocity fluctuations. The velocity energy spectra exhibited no notable buoyancy influence such as that in figure 18, and the energy-transfer mechanisms did not appear to be very sensitive to the buoyancy effects. The large differences in the important parameters chosen for the simulations and the available experiments may be partially seen in the lengthscale evolution maps for the simulations in figure 22. For the simulation with the smaller N, the initial buoyancy length was only twice as large as the initial overturning scale, while in the simulation with the larger N the initial buoyancy scale was chosen to be at least 50 % smaller than the initial overturning scale. Hence buoyancy effects should be important throughout the decay. The oscillatory behaviour of L_b in the simulations is similar to that occurring after the transition to an internal-wave field in the experiments. The relative size of the Kolmogorov scale brings out another important difference between the simulations and experiments. The values of $15.4L_K$ are larger than all the other lengthscales throughout the decay, so that viscous effects must also be important over the entire range of lengthscales in the turbulence. Despite these differences, these results show the potentially great value of detailed comparison of experiments and numerical

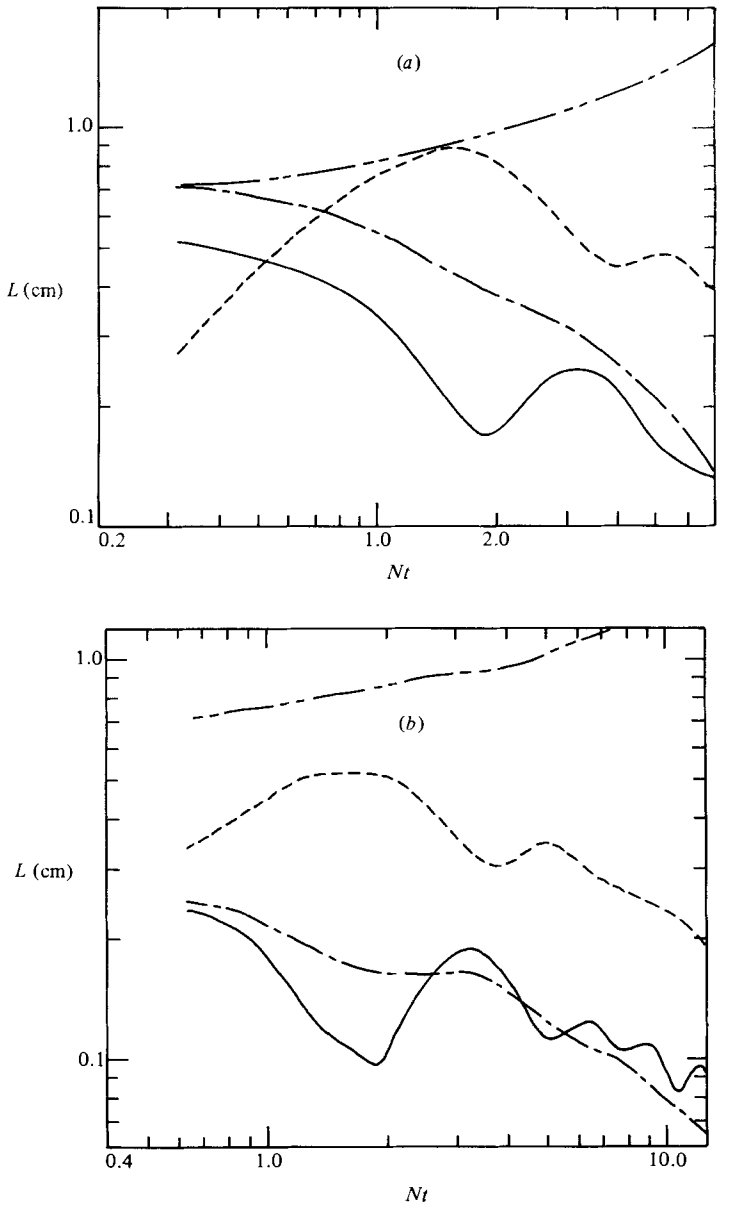

FIGURE 22. Lengthscale maps for the numerical simulations of Riley *et al.* (1981): (*a*) $N = 1.57$ rad/s, (*b*) $N = 3.14$ rad/s; ——, L_b; – – –, 1.4 L_R; – – – –, 15.4 L_K.

simulations of the evolution of density-stratified turbulent flows, and suggest future cooperation in designing both experiments and simulations with as nearly similar input and initial parameters as possible.

7. Conclusions

The decay of grid-generated turbulence in stably stratified salt water was investigated in a continuous-loop stratified water channel, and the results were compared to similar non-stratified experiments. Sufficiently energetic stratified turbulent flows

are observed to exhibit initial decay patterns as in non-stratified flows, with deviations from this decay occurring when inertial forces associated with the large scales become of the same order as the local buoyancy forces.

Spectra of the vertical velocity flucuations reveal that the large scales are suppressed first, while smaller scales remain energetic. These small scales exhibit classical turbulent behaviour and scale universally with Kolmogorov length- and velocity scales. As the motion continues to decay, a state is reached where all scales are affected by buoyancy, and classical turbulent universal similarity fails everywhere. During transition decreasing values of the vertical mass flux $\overline{\rho w}$ are observed, suggesting that the buoyancy-affected scales are not capable of overturning or entraining fluid at these scales (i.e. mixing), while smaller embedded motions continue to mix fluid. The vertical mass flux eventually becomes very small, indicating that the original turbulent field has been converted to random interval-wave motions.

At any particular time during the transition the buoyancy field is never as efficient at removing energy as viscous dissipation, with maximum efficiency near 20% indicated in the present set of experiments. However, depending on the initial energetics of the system, various degrees of permanent mixing result such that significant restratification can occur. For quickly damped turbulence much of the energy passed to the potential-energy field is released due to incomplete mixing and significant negative mass fluxes result that can be large relative to the local dissipation.

The duration of the transition period from the onset of buoyancy effects until only wave motions persist is found to be of the order of 0.15 Väisälä periods, which is less than the characteristic time of the turbulence based on the largest-scale eddies found in the flow at the onset of transition. This is consistent with the finding of Lange (1974), who observed 'collapse' of turbulent motions within one overturning of the energy-containing eddies.

A quantitative criterion for the existence of turbulence in a stratified fluid was determined based on the Stewart (1969) proposal that $\overline{\rho w} \to 0$ when turbulence ceases. For three values of N, we find $\epsilon_t = (24.5 \pm 0.5)\, \nu N^2$, as compared with the Gibson (1980) proposal that $\epsilon_t = 30 \nu N^2$. The present results suggest that active turbulence will exist at scales L in a stratified fluid if

$$L_b \approx 1.4 L_R > L > 15.4 L_K.$$

The lengthscale arguments of Ozmidov (1965) and others, and corresponding estimates of proportionality constants by Gibson (1980, 1981) are generally consistent with the results of our measurements.

This research was supported by the National Science Foundation principally under Grants OCE78-09060 and OCE82-05946 and in part by Grants CME78-25088 and MEA81-00431.

Appendix. Dissipation rates

Dissipation rates necessary to form several of the lengthscales were calculated from the spectra of the time series for u and w of the fluctuating velocity field. For homogeneous isotropic turbulence

$$\epsilon = \frac{\nu}{2}\overline{\left(\frac{\partial u_i}{\partial x_j} + \frac{\partial u_j}{\partial x_i}\right)^2} = \nu\overline{\left(\frac{\partial u_i}{\partial x_j}\frac{\partial u_i}{\partial x_j}\right)} = 15\nu\overline{\left(\frac{\partial u}{\partial x}\right)^2}.$$

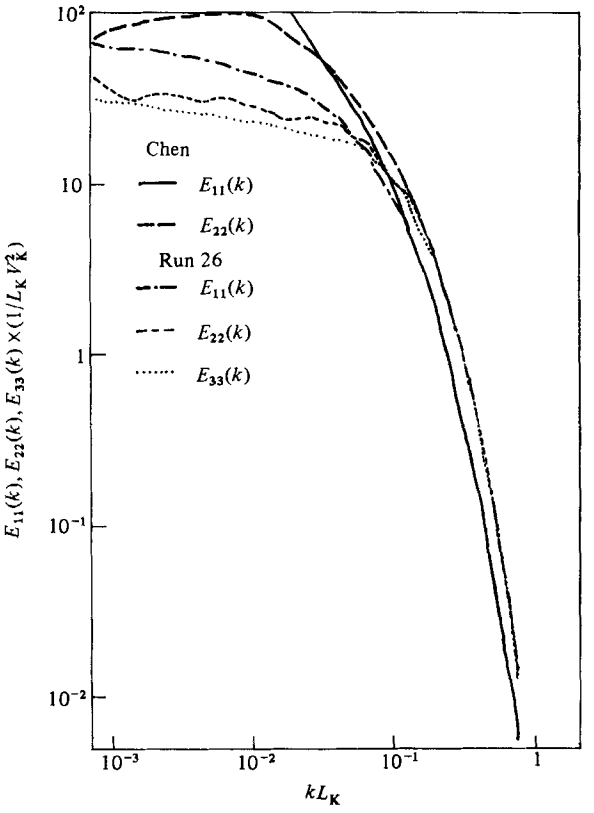

FIGURE 23. Normalized velocity spectra illustrating universal similarity at $x/M = 20$ for a non-stratified uniform-velocity flow, run 26.

Since both $\overline{(\partial u/\partial x)^2}$ and $\overline{(\partial w/\partial x)^2}$ can be obtained from the X-film spectral data and since isotropy of the velocity field may be affected by the stratification, all dissipation rates were formed using both moments, obtained from integrals of the second moments of the spectra. The dissipation rate was then evaluated as

$$\epsilon = \nu\left[10\overline{\left(\frac{\partial u}{\partial x}\right)^2} + \frac{5}{2}\overline{\left(\frac{\partial w}{\partial x}\right)^2}\right].$$

A major concern in deriving ϵ is to determine if the probes used to acquire the desired information can adequately resolve the signal. Since ϵ is dependent on the highest wavenumbers in the flow there is concern whether ϵ-calculations are underestimated owing to spatial resolution of the X-films.

Based on calculations by Wyngaard (1968), the DISA X-films, with sensor lengths of 1.1 mm separated 1.6 mm apart, generated measured spectral levels that were 3 dB down at wavenumbers near $k = 57$ cm^{-1} for the longitudinal spectra and 26 cm^{-1} for the vertical spectra. Uncorrected spectra taken directly behind the grid where the Kolmogorov lengthscale $L_K = (\nu^3/\epsilon)^{\frac{1}{4}}$ is smallest resulted in dissipation calculations about 15% lower than values boosted using Wyngaard's calculations.

For all the experiments spectra plots were boosted using Wyngaard's corrections, smoothed, and high-wavenumber noise regions rejected before integration of the data. All dissipation rates as well as the calculated lengthscales based on ϵ appear in table 4.

To verify experimentally that the velocity probes were correctly resolving the smallest scales necessary to compute ϵ correctly, several power spectra were plotted

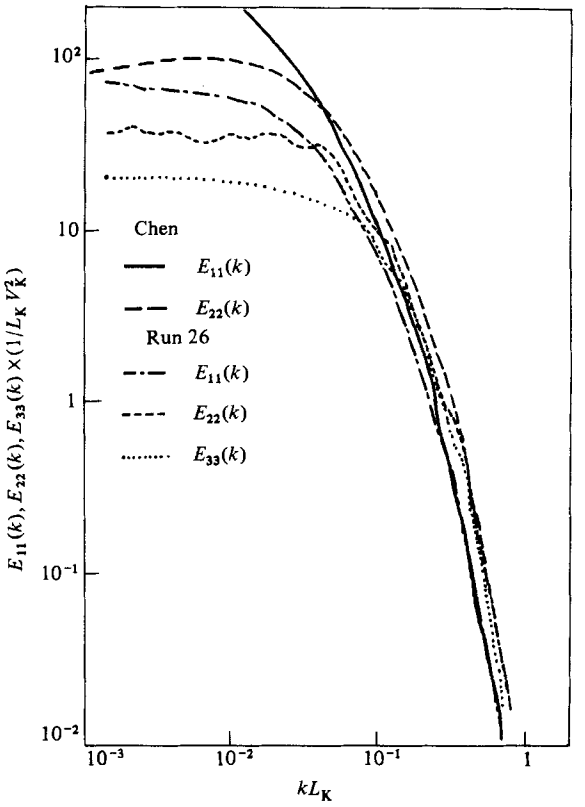

FIGURE 24. Normalized velocity spectra illustrating universal similarity at $x/M = 60$ for a non-stratified uniform flow, run 26.

in non-dimensional form based on Kolmogorov length- and velocity scales. According to Kolmogorov's first similarity hypothesis the non-dimensional form should be universal. Figures 23 and 24 show wind-tunnel grid data from Chen (1970) for $\overline{U} = 15.7$ m/s and 7.7 m/s, and the three 1-dimensional power spectra $E_{11}(k)$, $E_{22}(k)$, $E_{33}(k)$ from run 26, the non-stratified experiment.

$E_{11}(k)$ and $E_{33}(k)$ are taken directly from the measurements, and $E_{22}(k)$ is generated using the continuity equation and assuming the turbulence to be isotropic (Chen 1970):

$$E_{22}(k) = \frac{1}{2}\left[E_{11}(k) - k\frac{\mathrm{d}E_{11}(k)}{\mathrm{d}k}\right].$$

By generating $E_{22}(k)$ from $E_{11}(k)$ and comparing it with $E_{33}(k)$ one can determine over what wavenumber range the turbulence can be considered isotropic.

Figures 23 and 24 show that the grid produces classically shaped 1-dimensional spectra in the higher wavenumbers. The forms of $E_{11}(k)$ and $E_{33}(k)$ are different, as expected from continuity, with $E_{33}(k)$ greater than $E_{11}(k)$ at high wavenumbers and $E_{22}(k)$ being identical with $E_{33}(k)$ in this region, as predicted by isotropy.

Most importantly, these non-dimensional plots also show universal similarity with Chen's data, ensuring that the dissipation rates ϵ and Kolmogorov lengthscale L_K can be obtained correctly from the X-films.

Both plots show that isotropy and similarity hold at high wavenumbers downstream of the grid for non-stratified flows and therefore that measurements of ϵ and L_K for the mean speeds used in the facility are well resolved for all stations of interest.

REFERENCES

BATCHELOR, G. K. & TOWNSEND, A. A. 1948 Decay of isotropic turbulence in the initial period. *Proc. R. Soc. Lond.* **A 193**, 539.

CALDWELL, D. R., DILLON, T. M., BRUBAKER, J. M., NEWBERGER, P. A. & PAULSON, C. A. 1980 The scaling of vertical temperature gradient spectra. *J. Geophys. Res.* **85**, 1917.

CHEN, W. 1970 Spectral energy transfer and higher order correlations in grid turbulence. Ph.D. thesis, University of California, San Diego.

DICKEY, T. D. & MELLOR, G. L. 1980 Decaying turbulence in neutral and stratified fluids. *J. Fluid Mech.* **99**, 13.

DOUGHERTY, J. P. 1961 The anisotropy of turbulence at the meteor level. *J. Atmos. Terrest. Phys.* **21**, 210.

GIBSON, C. H. 1980 Fossil temperature, salinity and vorticity in the Ocean. In *Marine Turbulence* (ed. J. C. T. Nihoul), p. 221. Elsevier.

GIBSON, C. H. 1981 Fossil turbulence and internal waves. In *Non-linear Properties of Internal Waves* (ed. B. West). *AIP Conf. Proc.* no. 76.

GIBSON, C. H. 1982*a* Alternative interpretations for microstructure patches in the thermocline. *J. Phys. Oceanogr.* **12**, 374.

GIBSON, C. H. 1982*b* On the scaling of vertical temperature gradient spectra. *J. Geophys. Res.* **87**, 8031.

GREGG. M. C. 1980 Microstructure patches in the thermocline. *J. Phys. Oceanogr.* **10**, 915.

LANGE, R. E. 1974 Decay of turbulence in stratified salt water. Ph.D. thesis, University of California, San Diego.

LIN, T. J. & VEENHUIZEN, S. D. 1975 Measurements of the decay of grid-generated turbulence in a stratified fluid. *Flow Research Note* no. 85.

MILES, J. W. 1961 On the stability of heterogeneous shear flows. *J. Fluid Mech.* **10**, 496.

MONIN, A. S. & OBUKHOV, A. M. 1953 Dimensionless characteristics of turbulence in the surface layer of the atmosphere. *Dokl. Acad. Nauk SSSR* **92**, no. 2.

MONTGOMERY, R. D. 1974 An experimental study of grid turbulence in a thermally-stratified flow. Ph.D. thesis, University of Michigan.

NASMYTH, P. W. 1970 Oceanic turbulence. Ph.D. thesis, University of British Columbia.

OBUKHOV, A. M. 1959 On the influence of the buoyancy force on the structure of the temperature field in a turbulent flow. *Dokl. Acad. Nauk SSSR* **125**, no. 6.

OZMIDOV, R. V. 1965 On the turbulent exchange in a stably stratified ocean. *Atmos. Ocean Phys.* **8**, 853.

PAO, Y. H. 1973 Measurements of internal waves and turbulence in two-dimensional stratified shear flows. *Boundary-Layer Met.* **5**, 177.

RILEY, J. J., METCALF, R. W. & WEISSMAN, M. A. 1981 Direct numerical simulations of homogeneous turbulence in density-stratified fluids. In *Nonlinear Properties of Internal Waves* (ed. B. J. West). *AIP Conf. Proc.* no. 76.

STEWART, R. W. 1969 Turbulence and waves in a stratified atmosphere. *Radio Sci.* **4**, 1289.

STILLINGER, D. C. 1981 An experimental study of the transition of grid turbulence to internal waves in a salt-stratified water channel. Ph.D. thesis, University of California, San Diego.

STILLINGER, D. C., HEAD, M. J., HELLAND, K. N. & VAN ATTA, C. W. 1983 A closed-loop gravity-driven water channel for density-stratified shear flows. *J. Fluid Mech.* **131**, 73–89.

TAO, M. 1971 Turbulent mixing of density stratified fluids. Ph.D. thesis, University of Iowa.

WYNGAARD, J. C. 1968 Measurement of small scale turbulence structure with hot wires. *J. Sci. Instrum.* **2**, 1105.